Cryo-electron tomography of the apicomplexan invasion machinery in its native state reveals rigid body motion of the conoid and docked secretory machinery

Long Gui[1], William J. O'Shaughnessy[2], Kai Cai[1,#], Evan Reetz[1], Michael L. Reese[2,4,*], Daniela Nicastro[1,*]

[1]Department of Cell Biology, University of Texas, Southwestern Medical Center, Dallas TX USA

[2]Department of Pharmacology, University of Texas, Southwestern Medical Center, Dallas, TX USA

[4]Department of Biochemistry, University of Texas, Southwestern Medical Center, Dallas, TX USA

[#]Current address: Department of Biophysics, University of Texas, Southwestern Medical Center, Dallas, TX USA

*Address correspondence to Daniela Nicastro, daniela.nicastro@utsouthwestern.edu or to Michael L. Reese, michael.reese@utsouthwestern.edu

ORCIDs:

Daniela Nicastro: 0000-0002-0122-7173

Michael Reese: 0000-0001-9401-9594

Classification: BIOLOGICAL SCIENCES: Microbiology

Keywords: microtubule, cilium, apical complex, cryo-FIB

Short title: Structure of the apicomplexan invasion machinery

Abstract

The apical complex is a conserved cytoskeletal structure that organizes the secretory and invasion machinery of all apicomplexan parasites, the causative agents of diseases such as malaria, toxoplasmosis, and cryptosporidiosis. The structure of the apical complex and its mechanism of motion, which is thought to be required for host cell invasion, is not well understood. Recent advances in cryo-electron tomography (cryo-ET) have allowed the high-resolution reconstruction of large complexes in their near-native states. Here, we use cryo-focused ion beam milling to generate a thin specimen of the coccidian apical complex, allowing us to visualize and compare its three-dimensional structure in the protruded and retracted states *in situ* by cryo-ET. Subtomogram averaging of the 8 nm repeats from the conoid fibers (specialized microtubules) revealed their polarity and unusual nine-protofilament arrangement with associated proteins that connect and likely stabilize the fibers. In spite of the open shape of the conoid fibers, neither the structure of the conoid fibers nor the architecture of the spiral-shaped conoid complex as a whole are altered during cycles of protrusion and retraction. Thus the conoid moves as a rigid body, and is not compressible like a spring, as has been previously suggested. Instead, we found that the apical polar rings (APR), previously considered a rigid structure to which the conoid is docked, dilates during conoid protrusion. Furthermore, we identified previously undescribed actin-like filaments connecting the conoid to the APR during protrusion, consistent with a role of actin in driving conoid movements. In addition, our data capture the parasites in the act of secretion during conoid extension, allowing us to identify a network of interactions between the apical complex cytoskeleton and the parasite's secretory machinery.

Introduction

All intracellular pathogens must accomplish entry into a new host cell. Apicomplexan parasites use an invasion machinery composed of a specialized cytoskeletal complex and secretory organelles. Collectively, this group of organelles is known as the apical complex. It is for this structure that the phylum Apicomplexa is named, which includes the causative agents of malaria, toxoplasmosis, and cryptosporidiosis. The apical complex is essential for parasite motility, and for invasion into and egress from host cells. Furthermore, mutations that disrupt the apical complex functions block the Apicomplexan lytic cycle, rendering them non-infectious (Long *et al.*, 2017a, 2017b; Tosetti *et al.*, 2019; O'Shaughnessy *et al.*, 2020).

Apicomplexan parasites belong to the eukaryotic super-phylum Alveolata, like ciliates and dinoflagellates. Common ultrastructural characteristics of this super-phylum include the cytoskeleton-supported vesicular structures that lie just basal to the plasma membrane and are known as alveoli (Satir and Wissig, 1982). In Apicomplexa these structures are called the inner membrane complex (IMC), which runs along the length of the parasite (Mann and Beckers, 2001; Anderson-White *et al.*, 2011; Ouologuem and Roos, 2014; Ferreira *et al.*, 2020). Apicomplexan parasites have two distinct sets of specialized organelles, called the micronemes and rhoptries, from which invasion factors and effector proteins are secreted (Boothroyd and Dubremetz, 2008; Besteiro *et al.*, 2011; Santos and Soldati-Favre, 2011). Although these secretory organelles are not broadly conserved among alveolates, recent work has demonstrated that secretion from the rhoptries is mediated by a complex that is conserved both in its structure and protein components in ciliates such as *Tetrahymena* and *Paramecium* (Aquilini *et al.*, 2021).

The apical complex itself is a ~250 nm long structure (~25% the length of an *E. coli*) composed of a series of rings organized around a central spiral of specialized tubulin fibers called the conoid and inside which secretory organelles are organized and prepared for secretion. Whereas the conoid fibers are composed of the same tubulin dimers that makes up the parasites subpellicular microtubules, they do not form close tubes (Hu *et al.*, 2002). Instead, the conoid fibers form an open "C"-shaped structure

(Hu *et al.*, 2002), and the conoid complex is highly dynamic and protrudes and retracts (Mondragon and Frixione, 1996) as the parasites secrete adhesins and other motility/invasion factors (Carruthers and Sibley, 1999; Del Carmen *et al.*, 2009). Remarkably, the apical complex appears to have evolved from a eukaryotic cilium, as it contains both tubulin and cilium-associated proteins (Hu *et al.*, 2006; Francia *et al.*, 2012; de Leon *et al.*, 2013; Wall *et al.*, 2016). In addition, the core of the apical complex, including the conoid and its specialized tubulin structures, is conserved not only throughout Apicomplexa (Bertiaux *et al.*, 2021; Koreny *et al.*, 2021) and in closely related free-living organisms (Portman *et al.*, 2014), but also in more distantly related Alveolata, such as dinoflagellates (Okamoto and Keeling, 2014). Thus the apical complex appears to be an ancient structure, of which the molecular composition, high-resolution structure, and mechanistic understanding of its functions are still largely a mystery.

Structural biology has long relied on a “bottom-up” approach in which individual proteins are purified and structurally characterized. The “cryo-EM revolution” has provided the opportunity to determine the native structures of large macromolecular complexes, often after purification from native sources (Bai *et al.*, 2015; Cheng *et al.*, 2015). Advances in cellular cryo-electron tomography (cryo-ET) takes this one step further, and allows “top-down” *in situ* analyses of cellular structures directly in their native context. Cellular cryo-ET is a powerful imaging technique that can reveal structural details with molecular resolution, but the suitable thickness of biological samples is limited to a few hundred nanometers (McIntosh *et al.*, 2005). Most intact eukaryotic cells are thicker than this. Therefore, previous cryo-ET studies of whole eukaryotic cells have imaged either naturally thin cell regions, such as lamellipodia (Medalia *et al.*, 2002) and cilia (Lin and Nicastro, 2018), or cells that were compressed due to embedding in a thin layer of ice (compression force by water surface tension) (Cyrklaff *et al.*, 2007; Kudryashev *et al.*, 2012). Thicker specimens can be made thin enough for cryo-ET either by frozen-hydrated sectioning using a knife – which is prone to cutting artifacts (Al-Amoudi *et al.*, 2005) – or using a focused ion beam (Marko *et al.*, 2007).

We have applied cryo-ET to the coccidian apicomplexan parasites *Toxoplasma gondii* and its

close relative *Neospora caninum.* Our study used mainly cryo-focused ion beam (cryo-FIB) milling of unperturbed cells embedded in thick ice to compare the coccidian apical complex in its protruded and retracted states *in situ,* without the compression and deformation artifacts that plague unmilled samples (Cyrklaff *et al.*, 2007; Kudryashev *et al.*, 2012; Sun *et al.*, 2022). Our tomographic reconstructions provide an unrivaled view of the apical complex structure. Subtomogram averaging of the conoid fibers allowed us to clearly demonstrate that, contrary to a popular hypothesis (Hu *et al.*, 2002; Sun *et al.*, 2022), the conoid is not spring-like, and does not deform during cycles of protrusion and retraction. We also observed filaments that extend between the conoid and the apical polar rings (APR) through which it moves, suggesting that polymerization of actin, or an actin-like protein, may play a role during driving conoid motion. Our data also provide an unprecedented view of the interactions between the parasite's secretory organelles and the apical complex cytoskeleton, which allowed observation of hitherto undescribed connections. Finally, we were able to capture the act of microneme fusion with the intact plasma membrane.

Together this work provides structural and mechanistic details for the apicomplexan invasion machinery, the apical complex. Because this complex is essential for apicomplexan parasite invasion, understanding the molecular basis of its function could reveal important new targets for therapeutic intervention for some of the world's most devastating diseases.

Results

Cryo-FIB-milling of intact parasites followed by cryo-electron tomography imaging yields 3D structure of the cells in their native state

The coccidian cytoskeleton appears remarkably well-preserved after detergent-extraction and negative-staining, which has led to many TEM studies of apicomplexan ultrastructure using this preparation method (Hu *et al.*, 2002; Long *et al.*, 2017a; Nagayasu *et al.*, 2017; O'Shaughnessy *et al.*, 2020). We first tested whether cryo-ET of detergent-extracted and then plunge-frozen *Toxoplasma* cells would allow us to gain an accurate 3D view, with improved resolution of the cytoskeletal

structures, as compared to conventional TEM of negative-stained (dried) samples. Although cryo-ET of detergent-treated samples reveal cytoskeletal assemblies such as the apical conoid and subpellicular microtubules at high contrast (Supplemental Figure S1), the tomograms also show artifacts from the detergent extraction as well as structural distortions (*e.g.,* flattening; compare Supplemental Figure S1E-F to S1G-H) that complicated gaining reliable structural information from these samples.

To obtain the least perturbed and highest quality samples, we plunge-froze intact and live parasites in a relatively thick layer of ice (to avoid cell flattening by water surface tension). We then used cryo-FIB milling to generate <200 nm thick lamella of the vitrified, but otherwise native, parasites. To generate these samples, we used the NC1 strain of *Neospora caninum*, which is a BSL1 organism closely related to the human pathogen *Toxoplasma gondii*. Just before plunge-freezing, extracellular parasites were either prepared in an intracellular-like buffer (Endo and Yagita, 1990) or incubated with 10 µm calcium ionophore for 10 min so that the majority of parasites have conoids in the retracted or protruded states (Mondragon and Frixione, 1996), respectively. The resulting cryo-tomograms reveal well-preserved structural details of the native parasite apical complex, including membranes, cytoskeletal assemblies, and organelles (Figure 1).

Structural organization of the apical cell region

We compared the architecture of the apical complex in two states: conoid protruded and retracted. In the protruded state (Figures 1 and 2), the pre-conoidal rings (PCRs) are the cytoskeletal structure closest to the apical plasma membrane (Figure 1A-E), followed by the associated conoid that consists of 14-15 conoid fibers arranged in a spiral (Figure 1A,B,B',F). Basal to the protruded conoid, the inner membrane complex (IMC) is clearly visible as a flat double membrane structure with associated densities just below the parasite plasma membrane (Figure 1A). Notably, our *in situ* cryo-ET reveals several (non-periodic) densities that bridge between the two membranes of the extended sheet-like IMC (Figure 1A), perhaps serving as "spacers" that constrain the distance between the membranes. The apical rim of the IMC sheet is attached to the apical polar rings (APRs; Figure 1A,G). Just beneath the IMC, 22 subpellicular microtubules extend basally from the APRs (Figure 1A,H).

Although the subpellicular microtubules and associated microtubule inner proteins (MIPs) are well-resolved in our cryo-tomograms, we have not focused on them here, because they have previously been analyzed in detail (Wang *et al.*, 2021).

Instead of the previously reported two PCRs (Hu *et al.*, 2002, 2006), we resolve three PCRs (Figure 1B-D'; Supplemental Figures S1A-C; S2): P1 is the most apical and smallest ring with 151 ± 6 nm diameter (n=4 cells) – which was likely overlooked in previous detergent-treated and negatively stained samples; P2 (middle) and P3 (basal) both seem to consist of two sub-rings with the following diameters (Figure 1B,C; Supplemental Figure S2): P2a – 178 nm, P2b – 217 nm, P3a/b 258 nm. In our tomograms, P2a appears periodic with ~46 subunits (Figure 1C-D'; Supplemental Figure S2). P2 and P3 are connected with regularly spaced linkers that are ~25 nm long (Figure 1B-D'; Supplemental Figure S2).

Super-resolution light microscopy has suggested components of the APR segregate into independent rings (Leung *et al.*, 2017), but these rings have been difficult to resolve with negative staining EM. In our tomograms, we can clearly resolve several ring-shaped structures near the apical rim of the IMC: two distinct APRs with similar diameters, *i.e.* the A1 ring (apical) and the thicker A2 ring (basal) that may consist of two closely stacked sub-rings A2a and A2b (Figure 1G, Supplemental Figure S3A-C). We also observe a ring of amorphous density (named here "amorphous APR-associated density" or AAD) that is located between the IMC and the tips of the subpellicular microtubules (Figure 1G,H; Supplemental Figures S1A, S3A-C). The AAD appears to be connected to the APR rings and has basal projections (21 nm wide and 64 nm long) that are sandwiched between adjacent subpellicular microtubules (Figure 1A,H). The AAD projections have not been reported from conventional EM studies, but have recently been observed in another cryo-ET study ("interspersed pillars" in (Sun *et al.*, 2022)). We observe the APRs, AAD ring, and AAD projections in tomograms of both the protruded and retracted conoid states. Interestingly, the AAD ring and projections appear preserved during detergent-extraction of the parasite cytoskeleton (Supplemental Figures S1A, S3A-B). This localization and biochemical behavior suggests that the AAD ring and projections may contain

components of the IMC apical cap, which have recently been localized by super-resolution light microscopy as interleaved between microtubules (O'Shaughnessy *et al.*, 2020; Tosetti *et al.*, 2020). However, in these studies, known apical cap proteins such as ISP1 and AC9 extend ~1 μm from the APR, far beyond the ~64 nm occupied by the AAD projections. Therefore the AAD ring and projections appear to be composed of proteins that have yet to be identified or precisely localized.

As compared to the protruded conoid state, the conoid fibers in the retracted state are tucked just basal to the APRs, and the PCRs are located slightly apical of the APR structures (Figure 3; Supplemental Figures S3, S4). Surprisingly, in contrast to the idea that the APR serves to strongly anchor the conoid in the parasite membrane, the protruded conoid never appears fully square to the APRs in our tomograms (Figures 1A,I; 2A,B; Supplemental S3D-F). Instead, the conoid appears able to "wobble" as it protrudes. To quantify this observation, we compared the distances between the apical rim of the IMC and the basal edge of the conoid from opposing sides in central slices through our tomograms (Figure 2A,B). We found that the difference between the opposing distances varied greatly between tomograms of the protruded state ($\Delta d = 52 \pm 12$ nm). We also observed that the conoid was not symmetrically aligned within the parasite even in the retracted states (Supplemental Figure S3D-F), though the difference in distances was less striking ($\Delta d = 10 \pm 4$ nm). These data are consistent with the idea that the conoid is "leashed" to the APRs and/or the apical rim of the IMC with the AAD by flexible and perhaps dynamic structures. Indeed, we frequently observed filamentous density between the APR region and the conoid fibers (Figures 1I, 2C,C'; Supplemental Figure S3G-H'). In our detergent-extracted samples, the conoid appears to have collapsed upon the APRs (Supplemental Figure S1), as is typically seen in similarly treated samples by negative staining EM (Hu *et al.*, 2002; Nagayasu *et al.*, 2017; O'Shaughnessy *et al.*, 2020). Such a collapsed structure incorrectly suggests that the APR and its connections to the conoid are much more rigid than we observe in our cryo-FIB-milled, but otherwise unperturbed, samples, which again highlights the value of our *in situ* analysis of the structures in their native states.

Previous studies showed that apicomplexan "gliding motility" is driven by treadmilling of actin

fibers between the IMC cytoskeleton and the parasite plasma membrane (Sibley *et al.*, 1998). Recently, an F-actin nanobody has been used to demonstrate that these actin fibers appear to nucleate at the conoid and are passed down the parasite as it moves (Tosetti *et al.*, 2019). We clearly observe filaments consistent in diameter with actin fibers (~8 nm diameter) extending from the conoid to connect with the APR region, near where the hand-off to the IMC-associated myosin network (Meissner *et al.*, 2002; Wetzel *et al.*, 2003) would be expected to occur (Figures 1I, 2C; Supplemental Figure S3G-H'). These filaments vary in length from 38 – 164 nm in our tomograms, suggesting they are dynamic in nature (Figures 1I 2C, Supplemental Figure S2G-H').

Conoid structure is unchanged during cycles of protrusion and retraction

As described below, the conoid fibers are unusual tubulin polymers in which the protofilaments form an open C-shaped cross-section (Figure 4). These fibers were initially described as wound in a "spring-like" structure (Hu *et al.*, 2002), leading to a model that the conoid motions were driven by a spring-like mechanism, involving cycles of deformation in the conoid structure followed by release. This hypothesis is made more attractive because of the conoid fibers unusual C-shape, which would be expected to be more compressible than closed microtubules. Prior to the development of cryo-FIB milling, electron microscopy and tomography analysis of the conoid required detergent extraction of the parasite membrane and/or cell flattening, which often result in structural artifacts during sample preparation (Supplemental Figure S1A-F,I). Our data of the apical complex in an unperturbed state allows us to unambiguously address dynamics of the conoid ultrastructure.

We reasoned that any gross ultrastructural change in the conformation of the conoid polymer would result in changes in the overall dimensions and architectures of the conoids. We therefore compared the dimensions of protruded and retracted conoids (Figure 3; Supplemental Figure S4). Neither the apical conoid diameters (244 ± 19 nm protruded vs. 236 ± 8 nm retracted), the basal diameters (350 ± 25 nm vs. 326 ± 7 nm), nor the conoid heights (277 ± 5 nm vs. 262 ± 13 nm) were significantly different between the two states (Figure 3E; Supplemental Figure S4A). Similarly, the angle of the conoid fibers relative to the PCRs, and the intervals between adjacent conoid fibers were

225 indistinguishable in the two states (Figure 3F-I). Furthermore, both the mean conoid fiber length and the distribution of lengths in the population were not significantly different between the protruded and retracted states (399 ± 37 nm vs. 405 ± 45 nm; Supplemental Figure S5A).

As the conoid protrudes, the relative position of the APR shifts from level with the PCRs to basal to the conoid (compare Figure 3A,C with 3B,D). Importantly, we observed no ultrastructural differences
230 in the conoid fibers when comparing the two states. However, the plasma membrane, the apical IMC regions, the AAD, and the APRs all change their position relative to the conoid and its associated PCRs between the protruded and retracted samples (Figure 3A-D). The positions of the APRs and AAD appear closely coupled to the apical rim of the IMC in our tomograms, which appears to flex apically in the protruded state. We therefore asked whether the APRs exhibited structural changes
235 correlated with conoid protrusion and retraction. We measured the diameters of the APRs from each of our tomograms and determined that there was a striking ~15% increase in diameter in the protruded versus retracted states (Figure 3K,L; Supplemental Figure S4B). In contrast to the APRs, the PCRs and conoid fibers showed no observable differences between the two states (Figure 3J,M, Supplemental Figure S4C).

240 *Molecular structure and polarity of the conoid fibers*

We next assessed the conoid fiber structure at a higher resolution by generating separate subtomogram averages of the conoid fibers from the protruded (Figure 4A) and retracted states (Figure 4B). Visually, the subtomogram averages of the conoid fibers from either state appear largely indistinguishable, and reveal the 9 tubulin protofilaments (Hu *et al.*, 2002), as well as distinct protein
245 densities decorating the fibers (Figure 4A,B). To better assess any variation between the two states, we fitted tubulin dimers into the two averaged cryo-ET maps using Chimera (Goddard *et al.*, 2007) (Figure 4C,D) with correlation-coefficients of ~0.9. We then overlaid the best-fit models of a single repeat of the conoid fiber from each state (Figure 4E). Consistent with the lack of difference between the shape of the entire conoid structure between the two states (Figure 3), each of the 9 protofilament
250 subunits appear positioned indistinguishably between the two states within the error of the data

(Figure 4E). Note that the three protofilament subunits with the highest RMSD in their overlay (PF5-7; Supplemental Figure S5C) are fitted in a lower resolution region of the averages.

Taken together, our data demonstrate that the conoid appears to move as a rigid body during protrusion and retraction, rather than as a conformationally deformable structure, and there is no obvious rearrangement of protofilaments within the conoid fibers during this process. Nevertheless, our *in situ* data corroborate that the conoid fibers form an unusual open C-shaped arrangement of 9 protofilaments (Hu *et al.*, 2002) that requires contacts distinct from a typical 13-protofilament MT (Figure 4H).

Having demonstrated that the conoid fibers do not undergo major conformational changes between the protruded and retracted states, we combined particles from both states to calculate a global average of the conoid fibers (Figure 4I-K). Consistent with a rigid structure, the resulting average of the two states shows markedly improved resolution of ~2.8 nm at the 0.5 FSC-criterion (or ~2.2 nm at the 0.143 FSC criterion; Supplemental Figure S5B) and reveals density coating both the external (MT-associated proteins; MAPs) and internal (MT inner proteins; MIPs) edges of the conoid fiber (Figure 4I-O). The MIP densities bridge multiple protofilaments (Figure 4I) and coat almost the entire inner surface of the conoid fiber. These contacts may help explain the apparent rigidity of the conoid fiber structure. The external surface of the conoid fibers also appears almost entirely decorated with MAPs. Associated with PF5-8 are two layers of MAPs, named here as “inner-layer arm” and “outer-layer arm” densities (IA and OA; Figure 4I-O). Additional MAPs include MAP1, 2, and 4 which are associated with PF1, 2, and 4 respectively. We also observe inner-junction MAP densities (IJ) that connect PF3 of one conoid fiber (n) with PF9 of the neighboring fiber (n+1; Figure 4I,I’,L-O; Supplemental Figure S4G-I). These inter-fiber contacts likely stabilize the spiral conoid structure and reinforce its rigidity. Most MAPs exhibit a clear 8 nm periodicity along the length of the conoid fiber (Figure 4J-M; Supplemental Figure S1J,K, S5E-F’).

Regular microtubules are helical assemblies that have a characteristic handedness, helical pitch, and polarity. For example, a typical 13-protofilament microtubule forms a straight polymer with a rise of

3 monomers (12 nm) per left-handed helical turn (a “13-3 helix”), or 0.92 nm rise per protofilament-to-protofilament contact. (Mandelkow *et al.*, 1986). Using the regularly spaced MAPs as a guide (Figure 4J,K) we were able to assign the pitch of the conoid fiber in longitudinal views (Figure 4F; Supplemental Figure S5E-F’). As the C-shaped conoid fibers are formed from an open, non-helical microtubule, we calculated only the protofilament-to-protofilament pitch. Our model indicates that the conoid fiber forms through a left-handed assembly – like a typical microtubule, but has an estimated pitch of ~1.5 nm protofilament-to-protofilament, which is ~1.6-fold larger than a typical microtubule (Figure 4F; Supplemental Figure S5E-F’). To determine the structural polarity of the conoid fiber, we performed a nine-fold average of the protofilaments (using the tangential/normal to the C-shape curvature of the fiber). The isosurface rendering of the 9-fold averaged protofilaments displayed a ‘clockwise skew’ viewed from the base, suggesting the minus ends of the conoid fiber are located at the base of the conoid complex (Figure 4G).

In situ cryo-ET of native cells reveals functional segregation of secretory organelles within the coccidian conoid

Conventional EM of chemically-fixed and resin-embedded apicomplexan parasites has provided a basic overview of the organization of the apical secretory organelles within the coccidian conoid (Hu *et al.*, 2002; Paredes-Santos *et al.*, 2012), which we used to guide our analysis of the *in situ* structure of the apical complex in our tomograms (Figures 5 and 6). We clearly observe the central pair of intraconoidal microtubules (ICMT), extending from the conoid tip basally for 500-800 nm (Figure 5A), which is longer than the 350 nm previously reported (Hu *et al.*, 2002). The ICMT have been proposed to be a major organizing center for secretion in coccidia (Nichols and Chiappino, 1987; Carruthers and Sibley, 1997), and appear to have a set of associated proteins that are distinct from both the subpellicular microtubules and conoid fibers (Hu *et al.*, 2002), though only one such protein has been identified to date (Heaslip *et al.*, 2009).

Because of their short length and potential variation in their associated proteins along their length, subtomogram averaging of the ICMT did not yield sufficient resolution to clearly resolve MAPs or MIPs

(Figure 5C,D). Instead, we examined the chirality of the ICMT cross-section (Bouchet-Marquis *et al.*, 2007) using an ICMT subtomogram average from a detergent-extracted tomogram (Figure 5F). This analysis demonstrates that the ICMT, unlike the conoid fibers, have their minus-ends oriented apically. This observation suggests that the ICMT, unlike other apicomplexan MT structures, exhibits dynamic instability at its plus-end (Figure 5G), and may explain why the observed ICMT lengths vary largely between samples. We also observe a density that caps the apical, minus-end of the ICMT (Figure 5A,A'), which would be consistent with a microtubule-organizing center from which the ICMT are polymerizing. In coccidia, however, γ-tubulin appears to be restricted to the parasite centrioles and cytoplasm, and has not been localized to the apical complex (Morrissette and Gubbels, 2014). As has been previously reported (Paredes-Santos *et al.*, 2012), some ICMT contained a third microtubule (Figure 5E), suggesting that rigorous control of the structure is unnecessary for its function.

In line with what has been observed with EM of resin-embedded samples (Hu *et al.*, 2002), we observe that distinct secretory organelles (the rhoptries and micronemes) segregate to opposite sides of the ICMT (Figure 5A-B'). We also observed 4-6 regularly spaced vesicles tracking along one of the microtubules of the ICMT (Figures 5A-B;6A), consistent with previous reports (Paredes-Santos *et al.*, 2012; Aquilini *et al.*, 2021). We observed a single vesicle just apical of the ICMT that appears docked to the density of the recently described "rosette," and which has been associated with facilitating rhoptry secretion (Aquilini *et al.*, 2021). Consistent with this function, we observe that the membrane-docked vesicle connects to the apical tip of 1-2 rhoptries. We also identified clear densities connecting the vesicles to both the ICMT and to each other within a chain (Figures 5A; 6A). Notably, we did not observe this bridging density at the apical, membrane-docked vesicle (Figure 6A). Whereas the apical vesicle likely originated from the ICMT-associated vesicle chain, in docking with the rhoptry and plasma membrane, it appears to have been released from the vesicle-chain and its connections. We also observed that some of the vesicles appear elongated along the axis of the ICMT, suggesting that they are under tension and have been captured in active trafficking along the ICMT (Figure 5A).

A single parasite has ~10 rhoptries and tens of micronemes, though only a subset of either

organelle are docked at the parasite conoid at any given time (Paredes-Santos *et al.*, 2012). In all tomograms that contained the full diameter of the parasite conoid (6 of 9 tomograms), we observed 2 rhoptries tracking along the ICMT, but on opposite sides of the ICMT (Figure 5B,B'; colored pink). However, we do not observe clear linkers connecting the rhoptries to the ICMT. Within the apical region of the parasite, a helical density spirals along the rhoptry membranes (Figure 6B-C'), reminiscent of the localization pattern of Ferlin-2 seen by immuno-EM (Coleman *et al.*, 2018). The filaments spiraling up the rhoptries within the conoid were previously estimated to have a diameter of ~33 nm and a pitch of ~21.5 nm from tomograms of unmilled samples in which the parasites had been flattened due to surface tension (Mageswaran *et al.*, 2021). We found that such a predicted helix is consistent with our measurements of ~36 nm in diameter and ~17 nm in pitch from cryo-FIB-milled parasites (Figure 6C).

Notably, the ICMT and its associated vesicles and rhoptries segregates to one side of the conoid that is distinct from the region occupied by the micronemes (Figure 5A-B'), thus the ICMT is not directly involved in organizing micronemes for secretion. Nevertheless, the micronemes do not appear disorganized (Figure 6D,G,H). Instead, they are arrayed in clusters and show a distinct polarized orientation. The micronemes are relatively uniform in length (220±30 nm) and width (58±11 nm; Supplemental Figure S6), and the basal ends are rounded, whereas the apical ends appear narrow with a flattened, electron-dense cap (Figure 6D; inset). This density suggests an undescribed scaffolding complex that we propose organizes the micronemes and assists in their trafficking. In addition, we consistently identified a long filamentous density between the micronemes and the ICMT in each of our tomograms (Figure 5A,A'). These filaments are ~4 nm in width, consistent with a simple polymer, and could often be traced to extend from the top of the conoid to below its base. These data suggest that the filaments may assist in the organization and trafficking of the secretory organelles.

To initiate invasion of a host cell, all apicomplexan parasites rely on the secretion of a receptor/co-receptor pair comprising a microneme protein (AMA1) and a rhoptry proteins (RON2) (Lamarque *et al.*, 2011; Tyler and Boothroyd, 2011). Microneme and rhoptry components of the invasion apparatus

have been proposed to mix as they were secreted through a common path at the conoid (Boothroyd and Dubremetz, 2008). That we observe micronemes segregated from the docked rhoptries calls this model into question. Furthermore, in one tomogram of a protruded conoid, we identified a microneme that appears to have been captured in the process of plasma membrane docking/secretion (Figure 6E-F; Supplemental Figure S6J-N). We observe a density consistent with one large or multiple contact sites in a circular region ~85 nm diameter (Figure 6E, Supplemental Figure S6K-L). We also observe an apparent bolus of proteins on the surface of the plasma membrane associated with the contact site (Figure 6F, Supplemental Figure S6L), consistent with secretion of microneme contents. Notably, the docking site of this secreting microneme is 44 nm from the rosette and its docked rhoptry/apical vesicle, indicating that the two organelles secrete at separate sites using distinct secretory machineries. However, both the rhoptry-associated vesicle and the docked microneme were tethered to the same membrane-anchor and ridge (Figure 6E-F; Supplemental Figure S6J-N), which would likely facilitate spatial and temporal coordination of secretion.

Discussion

The conoid structure of the apical complex has captured the imagination of microscopists since its earliest descriptions by conventional TEM (Aikawa, 1967; de Souza, 1974). Here, we have applied cryo-ET to cryo-FIB-milled parasites to compare the native *in situ* structures of the coccidian apical complex cytoskeleton and associated secretory organelles in the protruded and retracted states of the conoid. Conoid protrusion is associated with striking morphological changes at the parasite apical tip that are visible by light microscopy (Mondragon and Frixione, 1996; Monteiro *et al.*, 2001). These morphological changes, coupled with the conoid's unusual spiral shape, has led to a model that the conoid is spring-like and deforms during its movements. Previous cryo-EM of detergent-extracted parasites (Leung *et al.*, 2020) and a recently published cryo-ET analysis (Sun *et al.*, 2022), document differences in protruded versus retracted conoids. However, subtomogram averaging in the Sun et al. study focused on detergent-extracted samples, and the samples used in both previous analyses were

compressed, which can lead to structural artifacts.

In contrast, our cryo-FIB-milled samples preserve the circularity of the coccidian apical complex structure (Supplemental Figure S1G-H), which allows more reliable interrogation of its native structure. Our data show that both the ultrastructure and molecular organization of the protruded and retracted states of the conoid are indistinguishable, indicating the conoid fibers do not deform like a spring during conoid movements, and therefore do not provide energy to assist in either conoid motion or in secretion.

Whereas we did not observe changes in the structure of the retracted versus protruded conoid, we found that the APR appears to dilate during protrusion which appears coupled with flexion of the IMC at the apical tip during protrusion. We also did not observe close contacts between the conoid and the APR, which instead appears to “wobble” within the apical space, consistent with flexible and/or dynamic tethers. RNG2 appears to be one such protein, as its N- and C-termini appear to span between the conoid and APR during protrusion (Katris *et al.*, 2014). While we would not expect to identify density of such an intrinsically disordered protein, we did observe densities that span between the base of the protruded conoid and the APR that were consistent with actin filaments. Therefore, it is possible that actin polymerization at this site is at least partially responsible for generating the force of conoid motion. Notably, an early description of conoid protrusion found that depolymerization of actin with cytochalisin D attenuated, but did not completely abrogate, conoid protrusion (Mondragon and Frixione, 1996). Nevertheless, further high resolution structural studies using genetic perturbation will be required to place individual proteins in the apical complex and tease apart the physical basis of the conoid dynamics and function.

Because our cryo-FIB-milled samples preserved the parasite membranes, we obtained an unparalleled view of the interactions between the cytoskeleton of the apical complex and the parasite’s specialized secretory organelles. We observed close contacts between the ICMT and both the parasite rhoptries and the apical vesicle chain. This suggests that the ICMT is responsible for organizing these organelles, but not the micronemes, with which we observed no direct contacts.

Intriguingly, while the ICMT are not broadly conserved in Apicomplexa outside of Sarcocystidae, a pair of ICMT have been reported in *Chromera velia* (Portman *et al.*, 2014), a free-living alveolate that is among the extant organisms most closely related to Apicomplexa. Thus, the ICMT may have been conserved in the ancestral species. That the apical vesicles and rhoptries track along the ICMT suggests that a microtubule motor may be facilitating their organization, though parasite kinesins and dyneins have not been localized to the ICMT. Because the majority of trafficking in Apicomplexa appears to occur on actin filaments (Jacot *et al.*, 2013; Periz *et al.*, 2019; Tosetti *et al.*, 2019; Carmeille *et al.*, 2021) the parasite microtubule motors have not yet been systematically characterized. Notably, only a single ICMT-localized protein has been identified to date (Heaslip *et al.*, 2009), which lacks clear homology to known structures.

A major open question in the field is the molecular basis of the force that drives the secretion of the invasion-associated organelles docked at the apical complex. The rhoptries are >1 μm in length, so would appear to require a more intricate machinery than simple membrane docking to drive secretion. Intriguingly, depolymerization of actin using cytochalasin D blocks parasite motility and invasion but not host cell attachment and rhoptry secretion (Håkansson *et al.*, 2001), suggesting actin is not responsible for driving secretion. Recent work identified the apicomplexan Nd proteins that comprise the “apical rosettes,” structures best characterized in the ciliate group of Alveolata (Plattner *et al.*, 1980). Similar to their role in ciliates, the *a*picomplexan Nd proteins are essential to rhoptry secretion (Aquilini *et al.*, 2021), and the rosette structure was recently described using unmilled cryo-ET (Mageswaran *et al.*, 2021). The *Toxoplasma* protein Ferlin-2 is also required for rhoptry secretion (Coleman *et al.*, 2018), and we and others (Mageswaran *et al.*, 2021) identified a helical density around the rhoptries within the conoid that is reminiscent of published Ferlin-2 immuno-EM staining pattern (Coleman *et al.*, 2018). These helical filaments may act somewhat like dynamin to squeeze the rhoptries during secretion. Among the *Toxoplasma* Nd-associated proteins were putative GTPase-related proteins (Aquilini *et al.*, 2021), suggesting a dynamin-like activity may be present at this site, as well.

We observed elongated fibers that track between the micronemes and the ICMT, and may represent cytoskeletal elements responsible for organization and trafficking of these organelles. While the diameter of the fibers is consistent with an actin-like filament, no such filament has been reported inside the conoid, likely because published studies on apically polymerized actin (Tosetti *et al.*, 2019) have not used imaging methods that could resolve actin inside the conoid versus along its surface. Microneme turnover requires trafficking along actin, though biogenesis and organization of micronemes appear actin-independent (Periz *et al.*, 2019). Further studies will be required to identify the molecular components of these fibers and their functions in organellar trafficking and secretion. Finally, with the ability to capture the cellular dynamics of active secretion, we were able to observe a docked microneme in the process of secretion. We found that the site of microneme secretion is distinct from that of a docked rhoptry, suggesting that the components of the invasion machinery secreted by these two organelles must find each in the apical plasma membrane after secretion. Finally, our data unambiguously show that microneme secretion can occur during conoid protrusion, events that have been indirectly correlated by other studies (Carruthers and Sibley, 1999). Note however, that these data do not rule out additional secretion during the retracted state.

In summary, cryo-ET of cryo-FIB-milled parasites has enabled us to examine the apical complex *in situ*, overcoming the compression artifacts that occur when preparing cells in a thin layer of ice. These significant advances allowed us to interrogate the native structure of the apical complex and its movements during retraction and protrusion. We were able to unambiguously demonstrate that the conoid moves as a rigid body during protrusion, with filamentous, actin-like projections that connect it to the APR. We anticipate that further studies combining proteomic data with cryo-ET of cryo-FIB-milled parasites will enable the placement of individual proteins into the apical complex structure, which will shed new light onto the molecular and structural basis of its movements and function.

Materials and Methods

Cell culture and cryo-preparation

Human foreskin fibroblasts (HFF) were grown in Dulbecco's modified Eagle's medium supplemented with 10% fetal bovine serum and 2 mM glutamine. *Toxoplasma gondii* (RH strain) and *Neospora caninum* (NC1 strain) tachyzoites were maintained in confluent monolayers of HFF. For preparation of parasites for cryo-ET, highly infected monolayers were mechanically disrupted by passage through a 27 gauge needle to release the parasites. For "retracted conoid" samples, parasites were kept in "Endo Buffer" (44.7 mM K_2SO_4, 10 mM $MgSO_4$, 106 mM sucrose, 5 mM glucose, 20 mM Tris-H_2SO_4, 3.5 mg/mL BSA, pH to 8.2 with H_2SO_4), which preserves the parasites in an intracellular-like state (Endo and Yagita, 1990). For "protruded conoid" samples, parasites were kept in HEPES pH 7.4 buffered saline. All parasites were passed through a 5 µm filter to remove cell debris washed in appropriate buffer and collected by centrifugation for 10 min at 300 g. Parasites were resuspended in the respective buffer and incubated for 10 min at 37°C with vehicle (retracted) or 10 µM calcium ionophore (protruded; A23187; Cayman Chemicals).

4 µl of the cultured cells were pipetted onto a glow-discharged (30 seconds at -30 mA) copper R2/2 holey carbon grid (Quantifoil Micro Tools GmbH, Jena, Germany). Samples were back-blotted with a Whatman filter paper (grade 1) for 3-4 s to remove excess liquid then the grid was quickly plunge frozen in liquid ethane using a homemade plunge freezer. For detergent-extracted samples, membranes were extracted by addition of Triton-X-100 in HBSS for 3-4 min before washing briefly in HBSS and back-blotting, as above. Vitrified grids were mounted in notched Autogrids for cryo-FIB-milling (Thermo Fisher Scientific, MA, USA) and stored in liquid nitrogen until used.

Cryo-FIB milling

Cryo-FIB milling was performed as previously described (Hariri *et al.*, 2019). Briefly, Autogrids with vitrified *N. caninum* cells were loaded into a shuttle and transferred into an Aquilos dual-beam instrument (FIB/SEM; Thermo Fisher Scientific) equipped with a cryo-stage that is pre-cooled to minus 185 °C. Tile-set images of the grid were generated in SEM mode, and the cells suitable for cryo-FIB

milling were targeted using the Maps software (Thermo Fisher Scientific). To protect the specimen and enhance conductivity, the sample surface was sputter-coated with platinum for 20 s at minus 30 mA current and then coated with a layer of organometallic platinum using the gas injection system pre-heated to 27°C for 5 s at a distance of 1 mm before milling (Schaffer *et al.*, 2017). Bulk milling was performed with a 30 kV gallium ion beam of 50 pA perpendicular to the grid on two side of a targeted cell. Then, the stage was tilted to 10°-18° between the EM grid and the gallium ion beam for lamella milling. For rough milling, the cell was milled with 30 kV gallium ion beams of 30 pA current, followed by 10 pA for polishing until the final lamella was 150 – 200 nm thick. The milling process was monitored by SEM imaging at 3 keV and 25 pA.

Cryo-ET imaging

Cryo-FIB milled lamellae of vitrified apical regions of the parasites were imaged using a 300 keV Titan Krios transmission electron microscope (Thermo Fisher Scientific) equipped with a Bioquantum post- column energy filter (Gatan, Pleasanton, CA) used in zero-loss mode with a 20 eV slit width and a Volta Phase Plate with -0.5 µm defocus (Danev *et al.*, 2017). The microscope control software SerialEM was utilized to operate the Krios and collect tilt series from 56° to -56° in 2° increments using a dose-symmetric tilting scheme in the lose-dose mode (Mastronarde, 2005; Hagen *et al.*, 2017). Images were captured using a 5k × 6k K3 direct electron detection camera (Gatan) at a magnification of 26,000x (3.151 Å pixel size). Counting mode of K3 camera were used and for each tilt image 15 frames (0.04 s exposure time per frame, dose rate of ~28 e/pixel/s; frames were recorded in super-res mode and then binned by 2) were captured. The total electron dose per tilt series was limited to 100 e/Å^2.

Data processing and figure generation

The frames of each tilt series image were motion-corrected using MotionCor2 and then merged using the script extracted from the IMOD software package (Kremer *et al.*, 1996) to generate the final

tilt serial data set. Tilt series images were aligned either fiducial-less using patch tracking (800 × 800-pixel size) or using dark features as fiducials (*e.g.* granules from the sputter coat or embedded Gallium from the milling process) using the IMOD software package. Tomographic reconstructions were calculated using both weighted back-projection for subtomogram alignment and averaging, and the simultaneous iterative reconstruction technique for reconstructions with higher contrast for particle picking. Subtomograms that contain the conoid fiber or the ICMT repeats were manually tracked and extracted from the raw tomograms, aligned, and averaged with missing wedge compensation using the PEET program (Nicastro *et al.*, 2006; Heumann *et al.*, 2011). 1160 and 721 8-nm conoid fiber repeats were selected from the protruded and retracted conoid tomograms, respectively, and 386 8-nm ICMT repeats were picked from the reconstructed tomograms.

Tomographic slices (without subtomogram averaging) were denoised for improved clarity using either non-linear anisotropic diffusion or a weighted median filter (smooth filter) implemented in IMOD. Isosurface renderings and cellular segmentation with manual coloring were generated using the UCSF Chimera package software (Pettersen *et al.*, 2004), which was developed by the Resource for Biocomputing, Visualization, and Informatics at the University of California, San Francisco, with support from NIH P41-GM103311.

Acknowledgments

We thank Daniel Stoddard for training and management of the cryo-electron microscopy facility at the University of Texas, Southwestern Medical Center, which is supported in part by the CPRIT Core Facility Support Award RP170644. This research was supported in part by the computational resources provided by the BioHPC supercomputing facility located in the Lyda Hill Department of Bioinformatics, UT Southwestern Medical Center. This work was supported by the National Institutes of Health (NIH; R01GM083122 to D.N., and R01AI150715 to M.L.R), the Cancer Prevention and Research Institute of Texas (CPRIT; RP140082 to D.N.), the National Science Foundation (MCB1553334 to M.L.R.), and the Welch Foundation (I-2075-20210327 to M.L.R.).

535

References

Aikawa, M (1967). Ultrastructure of the pellicular complex of Plasmodium fallax. J Cell Biol 35, 103–113.

Al-Amoudi, A, Studer, D, and Dubochet, J (2005). Cutting artefacts and cutting process in vitreous sections for cryo-electron microscopy. J Struct Biol 150, 109–121.

Anderson-White, BR, Ivey, FD, Cheng, K, Szatanek, T, Lorestani, A, Beckers, CJ, Ferguson, DJP, Sahoo, N, and Gubbels, M-J (2011). A family of intermediate filament-like proteins is sequentially assembled into the cytoskeleton of Toxoplasma gondii. Cell Microbiol 13, 18–31.

Aquilini, E et al. (2021). An Alveolata secretory machinery adapted to parasite host cell invasion. Nat Microbiol 6, 425–434.

Bai, X, McMullan, G, and Scheres, SHW (2015). How cryo-EM is revolutionizing structural biology. Trends Biochem Sci 40, 49–57.

Bertiaux, E, Balestra, AC, Bournonville, L, Louvel, V, Maco, B, Soldati-Favre, D, Brochet, M, Guichard, P, and Hamel, V (2021). Expansion microscopy provides new insights into the cytoskeleton of malaria parasites including the conservation of a conoid. PLoS Biol 19, e3001020.

Besteiro, S, Dubremetz, J, and Lebrun, M (2011). The moving junction of apicomplexan parasites: a key structure for invasion. Cell Microbiol 13, 797–805.

Boothroyd, JC, and Dubremetz, J-F (2008). Kiss and spit: the dual roles of Toxoplasma rhoptries. Nat Rev Microbiol 6, 79–88.

Bouchet-Marquis, C, Zuber, B, Glynn, A-M, Eltsov, M, Grabenbauer, M, Goldie, KN, Thomas, D, Frangakis, AS, Dubochet, J, and Chrétien, D (2007). Visualization of cell microtubules in their native state. Biol Cell 99, 45–53.

Carmeille, R, Schiano Lomoriello, P, Devarakonda, PM, Kellermeier, JA, and Heaslip, AT (2021). Actin and an unconventional myosin motor, TgMyoF, control the organization and dynamics of the endomembrane network in Toxoplasma gondii. PLoS Pathog 17, e1008787.

Carruthers, VB, and Sibley, LD (1997). Sequential protein secretion from three distinct organelles of Toxoplasma gondii accompanies invasion of human fibroblasts. Eur J Cell Biol 73, 114–123.

Carruthers, VB, and Sibley, LD (1999). Mobilization of intracellular calcium stimulates microneme discharge in Toxoplasma gondii. Mol Microbiol 31, 421–428.

Cheng, Y, Grigorieff, N, Penczek, PA, and Walz, T (2015). A primer to single-particle cryo-electron microscopy. Cell 161, 438–449.

Coleman, BI, Saha, S, Sato, S, Engelberg, K, Ferguson, DJP, Coppens, I, Lodoen, MB, and Gubbels, M-J (2018). A Member of the Ferlin Calcium Sensor Family Is Essential for Toxoplasma gondii Rhoptry Secretion. MBio 9.

Cyrklaff, M, Kudryashev, M, Leis, A, Leonard, K, Baumeister, W, Menard, R, Meissner, M, and Frischknecht, F (2007). Cryoelectron tomography reveals periodic material at the inner side of subpellicular microtubules in apicomplexan parasites. J Exp Med 204, 1281–1287.

Danev, R, Tegunov, D, and Baumeister, W (2017). Using the Volta phase plate with defocus for cryo-EM single particle analysis. ELife 6, e23006.

Del Carmen, MG, Mondragón, M, González, S, and Mondragón, R (2009). Induction and regulation of conoid extrusion in Toxoplasma gondii. Cell Microbiol 11, 967–982.

Endo, T, and Yagita, K (1990). Effect of extracellular ions on motility and cell entry in Toxoplasma gondii. J Protozool 37, 133–138.

Ferreira, JL, Heincke, D, Wichers, JS, Liffner, B, Wilson, DW, and Gilberger, T-W (2020). The Dynamic Roles of the Inner Membrane Complex in the Multiple Stages of the Malaria Parasite. Front Cell Infect Microbiol 10, 611801.

Francia, ME, Jordan, CN, Patel, JD, Sheiner, L, Demerly, JL, Fellows, JD, de Leon, JC, Morrissette, NS, Dubremetz, J-F, and Striepen, B (2012). Cell division in Apicomplexan parasites is organized by a homolog of the striated rootlet fiber of algal flagella. PLoS Biol 10, e1001444.

Goddard, TD, Huang, CC, and Ferrin, TE (2007). Visualizing density maps with UCSF Chimera. J Struct Biol 157, 281–287.

Hagen, WJH, Wan, W, and Briggs, JAG (2017). Implementation of a cryo-electron tomography tilt-scheme optimized for high resolution subtomogram averaging. J Struct Biol 197, 191–198.

Håkansson, S, Charron, AJ, and Sibley, LD (2001). Toxoplasma evacuoles: a two-step process of secretion and fusion forms the parasitophorous vacuole. EMBO J 20, 3132–3144.

Hariri, H et al. (2019). Mdm1 maintains endoplasmic reticulum homeostasis by spatially regulating lipid droplet biogenesis. J Cell Biol 218, 1319–1334.

Heaslip, AT, Ems-McClung, SC, and Hu, K (2009). TgICMAP1 is a novel microtubule binding protein in Toxoplasma gondii. PloS One 4, e7406.

Heumann, JM, Hoenger, A, and Mastronarde, DN (2011). Clustering and variance maps for cryo-electron tomography using wedge-masked differences. J Struct Biol 175, 288–299.

Hu, K, Johnson, J, Florens, L, Fraunholz, M, Suravajjala, S, DiLullo, C, Yates, J, Roos, DS, and Murray, JM (2006). Cytoskeletal components of an invasion machine--the apical complex of Toxoplasma gondii. PLoS Pathog 2, e13.

Hu, K, Roos, DS, and Murray, JM (2002). A novel polymer of tubulin forms the conoid of Toxoplasma gondii. J Cell Biol 156, 1039–1050.

Jacot, D, Daher, W, and Soldati-Favre, D (2013). Toxoplasma gondii myosin F, an essential motor for centrosomes positioning and apicoplast inheritance. EMBO J 32, 1702–1716.

Katris, NJ, van Dooren, GG, McMillan, PJ, Hanssen, E, Tilley, L, and Waller, RF (2014). The apical complex provides a regulated gateway for secretion of invasion factors in Toxoplasma. PLoS Pathog 10, e1004074.

Koreny, L et al. (2021). Molecular characterization of the conoid complex in Toxoplasma reveals its conservation in all apicomplexans, including Plasmodium species. PLoS Biol 19, e3001081.

Kremer, JR, Mastronarde, DN, and McIntosh, JR (1996). Computer visualization of three-dimensional image data using IMOD. J Struct Biol 116, 71–76.

Kudryashev, M, Münter, S, Lemgruber, L, Montagna, G, Stahlberg, H, Matuschewski, K, Meissner, M, Cyrklaff, M, and Frischknecht, F (2012). Structural basis for chirality and directional motility of Plasmodium sporozoites. Cell Microbiol 14, 1757–1768.

Lamarque, M et al. (2011). The RON2-AMA1 interaction is a critical step in moving junction-dependent invasion by apicomplexan parasites. PLoS Pathog.

de Leon, JC, Scheumann, N, Beatty, W, Beck, JR, Tran, JQ, Yau, C, Bradley, PJ, Gull, K, Wickstead, B, and Morrissette, NS (2013). A SAS-6-like protein suggests that the Toxoplasma conoid complex evolved from flagellar components. Eukaryot Cell 12, 1009–1019.

Leung, JM, He, Y, Zhang, F, Hwang, Y-C, Nagayasu, E, Liu, J, Murray, JM, and Hu, K (2017). Stability and function of a putative microtubule-organizing center in the human parasite Toxoplasma gondii. Mol Biol Cell 28, 1361–1378.

Leung, JM, Nagayasu, E, Hwang, Y-C, Liu, J, Pierce, PG, Phan, IQ, Prentice, RA, Murray, JM, and Hu, K (2020). A doublecortin-domain protein of Toxoplasma and its orthologues bind to and modify the structure and organization of tubulin polymers. BMC Mol Cell Biol 21.

Lin, J, and Nicastro, D (2018). Asymmetric distribution and spatial switching of dynein activity generates ciliary motility. Science 360, eaar1968.

Long, S, Anthony, B, Drewry, LL, and Sibley, LD (2017a). A conserved ankyrin repeat-containing protein regulates conoid stability, motility and cell invasion in Toxoplasma gondii. Nat Commun 8, 2236.

Long, S, Brown, KM, Drewry, LL, Anthony, B, Phan, IQH, and Sibley, LD (2017b). Calmodulin-like proteins localized to the conoid regulate motility and cell invasion by Toxoplasma gondii. PLoS Pathog 13, e1006379.

Mageswaran, SK, Guérin, A, Theveny, LM, Chen, WD, Martinez, M, Lebrun, M, Striepen, B, and Chang, Y-W (2021). In situ ultrastructures of two evolutionarily distant apicomplexan rhoptry secretion systems. Nat Commun 12, 4983.

Mandelkow, EM, Schultheiss, R, Rapp, R, Müller, M, and Mandelkow, E (1986). On the surface lattice of microtubules: helix starts, protofilament number, seam, and handedness. J Cell Biol 102, 1067–1073.

Mann, T, and Beckers, C (2001). Characterization of the subpellicular network, a filamentous membrane skeletal component in the parasite Toxoplasma gondii. Mol Biochem Parasitol 115, 257–268.

Marko, M, Hsieh, C, Schalek, R, Frank, J, and Mannella, C (2007). Focused-ion-beam thinning of frozen-hydrated biological specimens for cryo-electron microscopy. Nat Methods 4, 215–217.

Mastronarde, DN (2005). Automated electron microscope tomography using robust prediction of

specimen movements. J Struct Biol 152, 36–51.

McIntosh, R, Nicastro, D, and Mastronarde, D (2005). New views of cells in 3D: an introduction to electron tomography. Trends Cell Biol 15, 43–51.

Medalia, O, Weber, I, Frangakis, AS, Nicastro, D, Gerisch, G, and Baumeister, W (2002). Macromolecular architecture in eukaryotic cells visualized by cryoelectron tomography. Science 298, 1209–1213.

Meissner, M, Schlüter, D, and Soldati, D (2002). Role of Toxoplasma gondii myosin A in powering parasite gliding and host cell invasion. Science 298, 837–840.

Mondragon, R, and Frixione, E (1996). Ca(2+)-dependence of conoid extrusion in Toxoplasma gondii tachyzoites. J Eukaryot Microbiol 43, 120–127.

Monteiro, VG, de Melo, EJ, Attias, M, and de Souza, W (2001). Morphological changes during conoid extrusion in Toxoplasma gondii tachyzoites treated with calcium ionophore. J Struct Biol 136, 181–189.

Morrissette, N, and Gubbels, M-J (2014). Chapter 13 - The Toxoplasma Cytoskeleton: Structures, Proteins and Processes. In: Toxoplasma Gondii (Second Edition), ed. LM Weiss, and K Kim, Boston: Academic Press, 455–503.

Nagayasu, E, Hwang, Y-C, Liu, J, Murray, JM, and Hu, K (2017). Loss of a doublecortin (DCX)-domain protein causes structural defects in a tubulin-based organelle of Toxoplasma gondii and impairs host-cell invasion. Mol Biol Cell 28, 411–428.

Nicastro, D, Schwartz, C, Pierson, J, Gaudette, R, Porter, ME, and McIntosh, JR (2006). The molecular architecture of axonemes revealed by cryoelectron tomography. Science 313, 944–948.

Nichols, BA, and Chiappino, ML (1987). Cytoskeleton of Toxoplasma gondii. J Protozool 34, 217–226.

Okamoto, N, and Keeling, PJ (2014). The 3D structure of the apical complex and association with the flagellar apparatus revealed by serial TEM tomography in Psammosa pacifica, a distant relative of the Apicomplexa. PloS One 9, e84653.

O'Shaughnessy, WJ, Hu, X, Beraki, T, McDougal, M, and Reese, ML (2020). Loss of a conserved MAPK causes catastrophic failure in assembly of a specialized cilium-like structure in Toxoplasma gondii. Mol Biol Cell 31, 881–888.

Ouologuem, DT, and Roos, DS (2014). Dynamics of the Toxoplasma gondii inner membrane complex. J Cell Sci 127, 3320–3330.

Paredes-Santos, TC, de Souza, W, and Attias, M (2012). Dynamics and 3D organization of secretory organelles of Toxoplasma gondii. J Struct Biol 177, 420–430.

Periz, J, Del Rosario, M, McStea, A, Gras, S, Loney, C, Wang, L, Martin-Fernandez, ML, and Meissner, M (2019). A highly dynamic F-actin network regulates transport and recycling of micronemes in Toxoplasma gondii vacuoles. Nat Commun 10, 4183.

Pettersen, EF, Goddard, TD, Huang, CC, Couch, GS, Greenblatt, DM, Meng, EC, and Ferrin, TE (2004). UCSF Chimera--a visualization system for exploratory research and analysis. J Comput Chem

25, 1605–1612.

Plattner, H, Reichel, K, Matt, H, Beisson, J, Lefort-Tran, M, and Pouphile, M (1980). Genetic dissection of the final exocytosis steps in Paramecium tetraurelia cells: cytochemical determination of Ca2+-ATPase activity over performed exocytosis sites. J Cell Sci 46, 17–40.

Portman, N, Foster, C, Walker, G, and Šlapeta, J (2014). Evidence of intraflagellar transport and apical complex formation in a free-living relative of the apicomplexa. Eukaryot Cell 13, 10–20.

Santos, JM, and Soldati-Favre, D (2011). Invasion factors are coupled to key signalling events leading to the establishment of infection in apicomplexan parasites. Cell Microbiol 13, 787–796.

Satir, BH, and Wissig, SL (1982). Alveolar sacs of Tetrahymena: ultrastructural characteristics and similarities to subsurface cisterns of muscle and nerve. J Cell Sci 55, 13–33.

Schaffer, M, Mahamid, J, Engel, BD, Laugks, T, Baumeister, W, and Plitzko, JM (2017). Optimized cryo-focused ion beam sample preparation aimed at in situ structural studies of membrane proteins. J Struct Biol 197, 73–82.

Sibley, LD, Håkansson, S, and Carruthers, VB (1998). Gliding motility: an efficient mechanism for cell penetration. Curr Biol CB 8, R12-14.

de Souza, W (1974). Fine structure of the conoid of Toxoplasma gondii. Rev Inst Med Trop Sao Paulo 16, 32–38.

Sun, SY, Segev-Zarko, L-A, Chen, M, Pintilie, GD, Schmid, MF, Ludtke, SJ, Boothroyd, JC, and Chiu, W (2022). Cryo-ET of Toxoplasma parasites gives subnanometer insight into tubulin-based structures. Proc Natl Acad Sci U S A 119, e2111661119.

Tosetti, N, Dos Santos Pacheco, N, Bertiaux, E, Maco, B, Bournonville, L, Hamel, V, Guichard, P, and Soldati-Favre, D (2020). Essential function of the alveolin network in the subpellicular microtubules and conoid assembly in Toxoplasma gondii. ELife 9.

Tosetti, N, Dos Santos Pacheco, N, Soldati-Favre, D, and Jacot, D (2019). Three F-actin assembly centers regulate organelle inheritance, cell-cell communication and motility in Toxoplasma gondii. ELife 8.

Tyler, JS, and Boothroyd, JC (2011). The C-terminus of Toxoplasma RON2 provides the crucial link between AMA1 and the host-associated invasion complex. PLoS Pathog 7, e1001282.

Wall, RJ, Roques, M, Katris, NJ, Koreny, L, Stanway, RR, Brady, D, Waller, RF, and Tewari, R (2016). SAS6-like protein in Plasmodium indicates that conoid-associated apical complex proteins persist in invasive stages within the mosquito vector. Sci Rep 6, 28604.

Wang, X, Fu, Y, Beatty, WL, Ma, M, Brown, A, Sibley, LD, and Zhang, R (2021). Cryo-EM structure of cortical microtubules from human parasite Toxoplasma gondii identifies their microtubule inner proteins. Nat Commun 12, 3065.

Wetzel, DM, Håkansson, S, Hu, K, Roos, D, and Sibley, LD (2003). Actin filament polymerization regulates gliding motility by apicomplexan parasites. Mol Biol Cell 14, 396–406.

Figure Legends

Figure 1. Three-dimensional *in situ* architecture of the apicomplexan invasion machinery revealed by cryo-FIB milling and cryo-ET. (A) Tomographic slice of the reconstructed apical end of *N. caninum* with protruded conoid. Note the spacers connecting between the two membranes of the inner membrane complex (IMC, blue arrowheads). Other labels and coloring see below. In longitudinal views, apical is oriented towards the top of the images throughout the manuscript, unless otherwise noted. **(B-D')** Tomographic slices (B-D: originals; B'-D': pseudo-colored) of the same cell with protruded conoid that is visualized in (I), show the 3 layers of the pre-conoidal rings (PCR) associated with the conoid (orange). White lines in (B) indicate the positions of the cross-sectional views in (E and F). **(E, F)** Cross-sectional tomographic slices show the round PCR P2 ring (E) and the conoid complex composed of 15 CFs (F) without cell flattening. **(G)** A tomographic slice shows two distinct APR rings (red arrowheads) and the AAD ring (purple arrowhead) which is located between the APR and IMC. **(H)** Tomographic slice through a partially retracted conoid that was cryo-FIB milled cross-sectionally, clearly shows the SPMTs ending near the AAD ring and with AAD projections (purple arrows) interspersed between neighboring SPMTs. **(I)** 3D segmentation and visualization of the apical complex. Labels and colors used throughout the manuscript unless otherwise noted: AAD (purple), amorphous APR-associated density ring and projections; actin-like filaments (magenta); APR (red), apical rings; CF (orange), conoidal fiber; ICMT (light green), intraconoidal microtubules; IMC (cyan), inner membrane complex; PCR (yellow), three pre-conoidal rings (P1: blue, P2a/b: green, P3: yellow, regular linkers between P2 & P3: purple); PM (gray), plasma membrane; SPMT (green), subpellicular microtubules. Scale bars: 100 nm (in A, also valid in G & H); 50 nm (in B, also valid in C-F).

Figure 2. The protruded conoid "wobbles" on top of the APR. (A, B) Tomographic slices through the protruded conoid complex from 2 parasites. Measurements mark the minimum distances between the IMC and the conoid fibers on each side of the conoid. **(C, C')** Tomographic slice (C: original; C': pseudo-colored) shows filamentous densities (magenta) connect the conoid (orange) and the APR

(red). Arrowheads in C highlight regular connections between neighboring conoid fibers. Scale bar: 100 nm.

Figure 3. The overall structure of the conoid remains unchanged during the cycles of protrusion and retraction. (A-D') Tomographic slices through the center of the apical complex show the conoid in the protruded (A) and retracted (B) states. White lines indicate the measurements of the apical diameter (a), the basal diameter (b) and the height (h) of the conoid structure. White boxes in (A, B) indicate the areas magnified in (C, D) where the conoid and the APR-associated complex interact; (C' and D') are the pseudo-colored versions of (C, D). **(E)** Measurements of the apical diameter, the basal diameter and the height of protruded (white bars) and retracted (gray bars) conoids showed no significant changes during the cycles of protrusion and retraction. **(F-I)** Tomographic slices (F, G) through the top edge of reconstructed conoids (showing the conoid fibers in longitudinal section) in the protruded (F) and retracted (G) states. Lines indicate the measurement of the relative angle between the CFs and the PCR plane (red lines), and the measurement of the distance between neighboring CFs (blue lines); the results of latter measurement for protruded and retracted conoids is shown in (H) and (I), respectively. **(J-M)** Tomographic slices show representative PCRs (J and M) and APRs (K and L) in cross-sectional views of the apical complex in protruded (J,K) and retracted (L,M) states. Diameters of APR and PCR are indicated as ranges from all available tomograms (n=3 for APR in both states; n=3 PCR protruded; n=2 PCR retracted). Scale bars: 100 nm (in A, also valid in B, J, K, L & M); 50 nm (in C, also valid in D, F & G). Statistical significance was calculated by Student's t-test. n.s., not significant ($P > 0.05$).

Figure 4. Subtomogram averages of the conoid fibers show a C-shape architecture with nine tubulin protofilaments and associated proteins. (A, B) Tomographic slices of the averaged 8-nm repeats of the CF fibers in the protruded (A) and retracted (B) states. **(C-E)** The high-resolution structure of tubulin was fitted into the cryo-ET map in the protruded (C, blue) and the retracted (D,

590 pink) states. Comparison (E) of the two pseudo-atomic protofilament models in the protruded (blue) and retracted (pink) states shows no significant difference. **(F)** Longitudinal views of the pseudo-atomic protofilament model in the retracted state. The pitch was estimated based on the rise of the periodic CF-associated MAPs between neighboring protofilaments. **(G)** The arrangements of the modeled protofilaments in the CFs compared with the high-resolution cryo-EM structure of the typical
595 13-protofilament subpellicular microtubules (EMDB: EMD-23870). The most substantial difference is the angle change between PF4 and PF5, causing a tight kink in CFs. **(H)** Isosurface rendering of the nice-fold averaged protofilaments display a 'clockwise skew' when viewed from the conoid base, suggesting the minus ends of the conoid fiber are orientated to the base. **(I-K)** Tomographic slices of the global CF averages that combine all data from both the protruded (A) and retracted (B) states
600 viewed in cross-sectional (I: original; I': pseudo-colored) and longitudinal (K and L) orientations. The white lines in (I) indicate the locations of the slices in the respective panels. Labels and coloring see below. **(L-O)** Isosurface renderings show the 3D structures of the averaged repeats of a CF in cross-sectional (L) and longitudinal (M) views, as well as the CFs from a complete conoid (N) by assembling the 8-nm repeats back to the full tomogram. This and the zoom-in (O) show that the open face of the
605 CFs faces the interior of the conoid. Labels and coloring: 1-9, protofilaments; IA (blue) and OA (pink), "inner-layer arm" and "outer-layer arm" densities; IJ (yellow), inner junction MAP; MAP1 (orange), 2 (magenta), 4 (green), microtubule associated proteins. Scale bars: 10 nm (in A, also valid in B-D, I-K).

Figure 5. The apical secretory machinery is organized around the intra-conoidal microtubules.
610 **(A-B')** Tomographic slices (A, B: original; A', B': pseudo-colored) show the apical tip of a *N. caninum* cell with the secretory organelles organized around the ICMT inside the conoid complex in longitudinal (A) and cross-sectional (B) orientations. The long ICMTs connect the apex of the conoid to the cytosol, and closely co-localized with the secretory vesicles (light blue) and two rhoptries (rose). Other coloring: CFs (orange), micronemes (dark purple), filamentous density (magenta), inter-vesicular
615 connections (purple), "crowning" density of the ICMT (pink). **(C, D)** Slices of the averaged 8-nm

repeats of the ICMTs viewed in cross-sectional (C) and longitudinal (D) orientations. **(E)** Occasionally, more than two microtubules were observed in the ICMT complex. Shown here is an example of three microtubules (white arrowheads). **(F)** Thirteen-fold rotationally averaged ICMT from 53 tomograms of detergent-extracted *Toxoplasma* cells. The arrows indicate the clockwise skew of the protofilaments when the ICMT is viewed from apical to basal, indicating that the minus ends of the ICMTs are oriented apically in the parasite. **(G, G')** The basal ends of the ICMTs showed flared regions and different lengths of protofilaments, which is associated with the plus-end of growing MTs. Scale bars: 100 nm (in A); 50 nm (in B, also valid in E & G); 10 nm (in C, also valid in D & F).

Figure 6. The functional segregation of secretory organelles within the conoid complex revealed by cryo-FIB milling and cryo-ET. (A-C') Tomographic slices (A,B,C: original; A',B',C': pseudo-colored) show (A,A') 5 regularly spaced, oval-shaped vesicles (light blue) tracking along one of the microtubules of the ICMT (light green), (B, B') a rhoptry (pink) interacting with the plasma membrane (PM) via a vesicle (light blue) and the "rosette" docking complex (yellow), and (C, C') a helical scaffold (dark pink) associated with the rhoptry membrane. **(D)** The micronemes are organized in a group that occupies a region of the apical complex that is distinct from the region occupied by the ICMT associated vesicles and rhoptries. Insert: subtomogram average of 25 microneme apical tips show a flattened, electron dense cap. **(E, F)** Tomographic slices provide a side (E) and a top view (F) of two secretory organelles, a microneme (M) and a rhoptry-associated vesicle (V), that are docked side-by-side to the plasma membrane (the vesicle through the rosette (Ro)), but with distinct docking sites (44 nm apart). Note that both organelles are tethered (pink and blue arrows) to the same plasma membrane-anchored ridge (yellow arrows). The white line in (E) indicates the location of the slice in (F). **(G, H)** 3D segmentation and visualization of a tomogram showing the overall organization of secretory organelles within the conoid complex including micronemes (dark blue), rhoptries (rose), ICMT (green), vesicles (light blue) and inter-vesicular connections (purple), filamentous structure along micronemes (magenta), plasma membrane (gray). Scale bars: 50 nm (in A-C & E-F); 100nm (in

D); 20 nm (in D bottom-left insert).

Supplemental Figure Legends

Figure S1. Detergent-extracted *Toxoplasma* exhibits a flattened structure imaged by cryo-ET. **(A-D)** Tomographic slices of the apical complex of the detergent-extracted tachyzoite in longitudinal (A, B, D) and cross-sectional orientation (C). White lines in (A) indicate the positions of the cross-sectional views shown in (C and E). Note the periodic connections between neighboring CFs (orange arrowheads). Other labels and coloring as for Figure 1. White box in (A) indicates the region magnified and orientation-optimized in (B), showing the detailed PCR structure with three layers (P1-P3) and repeating densities connecting the layers. A cross-sectional view of PCR-P2 (C) reveals severe flattening of the detergent-extracted sample. The APR-region is shown in (D) with at least three layers of APRs (A1, A2a, A2b) and a ring of amorphous APR-associated density (AAD). **(E-H)** Comparison of tomographic slices (E, G) and graphical models (F, H) of cross-sectional views of the apical complex in a detergent-extracted, severely flattened and distorted *Toxoplasma* cell (E, F), and in a native, un-flattened *N. caninum* cell that was embedded in a relatively thick ice layer and cryo-FIB milled to avoid cell flattening (G, H). Viewed from the apical end; model points in (F, H) indicate repeat units of the CFs (orange arrowheads). **(I-K)** Cross-sectional and longitudinal tomographic slices (I: original, I': pseudo-colored) through the averaged 8-nm repeats of the conoid fibers in detergent-extracted apical complexes. Note that the resolution is relatively high in the longitudinal direction (J, K), but in cross-section (I), elongation due to the missing wedge artifact is apparent (flattening results in orientation bias of the CFs). Labels and coloring as in Figure 4. Scale bars: 100 nm (in A-E and G); 10 nm (in I, also valid in J and K).

Figure S2. Three rings were identified as components of the PCR. (A-H) Longitudinal (A, B) and cross-sectional tomographic slices (B-D & F-H) through the top of the apical complex in either protruded (A-D) or retracted states (E-H) reveal that the PCR is composed of at least three distinguishable annular structures that we name from apical to basal: P1 (blue), P2 – with an interior

P2a (green) and an exterior P2b (light green), and P3 (yellow). White lines in (A and E) indicate the positions of the corresponding cross-sectional views. Scale bars: 50 nm (in D & H, also valid in A-C & E-G).

Figure S3. Dynamic interactions between the APR and the conoid fibers. (A, B) Tomographic slices highlight the APR from a detergent-extracted *Toxoplasma* tachyzoite. **(C)** Cross-sectional tomographic slice of the APR in the partially retracted conoid from a cryo-FIB-milled *Neospora* tachyzoite. Red arrowhead indicates one of the annular rings of the APR, purple arrowhead and arrows indicate the AAD ring and AAD projections, respectively. **(D-F)** Tomographic slices through (cryo-FIB milled) conoid complexes in the retracted state. Measurements mark the closest distance between the IMC (cyan arrowheads) and the conoid fibers (orange arrowheads). **(G, H)** Tomographic slices (G, H: original: G', H': pseudo-colored) of protruded conoids show ~8 nm diameter filamentous densities of variable lengths (magenta) that appear to connect the conoid fibers (orange) to the APR (red). Note that the orientation of these filaments slightly varies within the 3D reconstructions, therefore it is impossible to capture all connections in full length in a single slice (see Figure 1I for example 3D rendering). Scale bars: 100 nm.

Figure S4. Image gallery of the conoid complex, APRs and PCRs in the protruded and retracted states. (A) Tomographic slices of the apical complex in the protruded and retracted states. Measurements indicate the apical diameter (a), the basal diameter (b) and the height (h) of the conoid structure. **(B, C)** Cross-sectional tomographic slices of the apical complex show the diameters of the APR (B) and the P2-PCR (C) in the protruded and retracted states. Scale bars: 100 nm (A & B); 50 nm (C).

Figure S5: Structural features of the subtomogram averages of the conoid fibers from cryo-FIB milled *Neospora* cells. (A) The lengths of the conoid fibers are unchanged between the protruded

and retracted states. Statistical significance was calculated by Student's t-test. n.s., not significant ($p > 0.05$). **(B)** Resolution estimate of the global* average of the conoid fiber was measured at the PF4 region using the Fourier shell correlation method (* combining tomograms from both protruded and retracted states). Dashed lines and values indicate where the FSC curve intersects with the 0.5 or 0.143 criteria. **(C)** RMSD values comparing the relative position and orientation of each protofilament in the pseudo-atomic models after fitting tubulin dimers to the averaged conoid fiber in the retracted and protruded states (see Figure 4A-D). **(D-F')** Cross-sectional (D) and longitudinal (E, F: original, E', F': annotated) tomographic slices of the global subtomogram average of the conoid fibers show the pitch (indicated by green lines) along neighboring MAPs (E) or MIPs (F). White lines in (D) indicate the positions of the longitudinal views in (E and F). **(G-I)** Tomographic slices through the conoid filaments (G) show the ~8-nm-spaced linkages (orange arrowheads) between adjacent conoid fibers. In cross-sectional (H) and longitudinal (I) tomographic slices of the global subtomogram average of the conoid fibers (H, I; depicted are three neighboring conoid fibers) these linkages can be seen as the inner junction (IJ) MAPs between PF3 of conoid fibers CF_n and PF9 of the neighboring CF_{n+1}. Scale bars: 10 nm (in D-F & H-I); 50 nm in G.

Figure S6. Micronemes inside the apical complex have a regular shape and size, and dock to the plasma membrane at sites distinct from but organized with the rhoptry-associated vesicle. (A-H) Representative tomographic slices of micronemes in cryo-FIB-milled *Neospora* tachyzoites highlight the fairly consistent shapes and polar morphology of these organelles; apical oriented towards the top. **(I)** Distribution of lengths and diameters of the micronemes from the cryo-ET reconstructions. Numbers are averages ± standard deviations (n=20 micronemes). **(J-N)** Tomographic slices provide side (J, M, N) and top views (K, L) of a microneme (M) and a rhoptry-associated vesicle (V) that are docked to the plasma membrane (PM) side-by-side (see also Figure 6E, F). The docking sites are distinct, i.e. the vesicle docks through the rosette (small dark spot in K) and the microneme via a contact site in a circular region of ~85 nm in diameter (L) to the plasma membrane. Nonetheless,

720 the location of docking appear to be organized in close proximity, likely through connections from the organelles (pink and blue arrows) to a long ridge (yellow arrows) that runs between the secretory organelles and is tethered to the plasma membrane. Scale bars: 50 nm (scale bar in A, also valid in B-H).

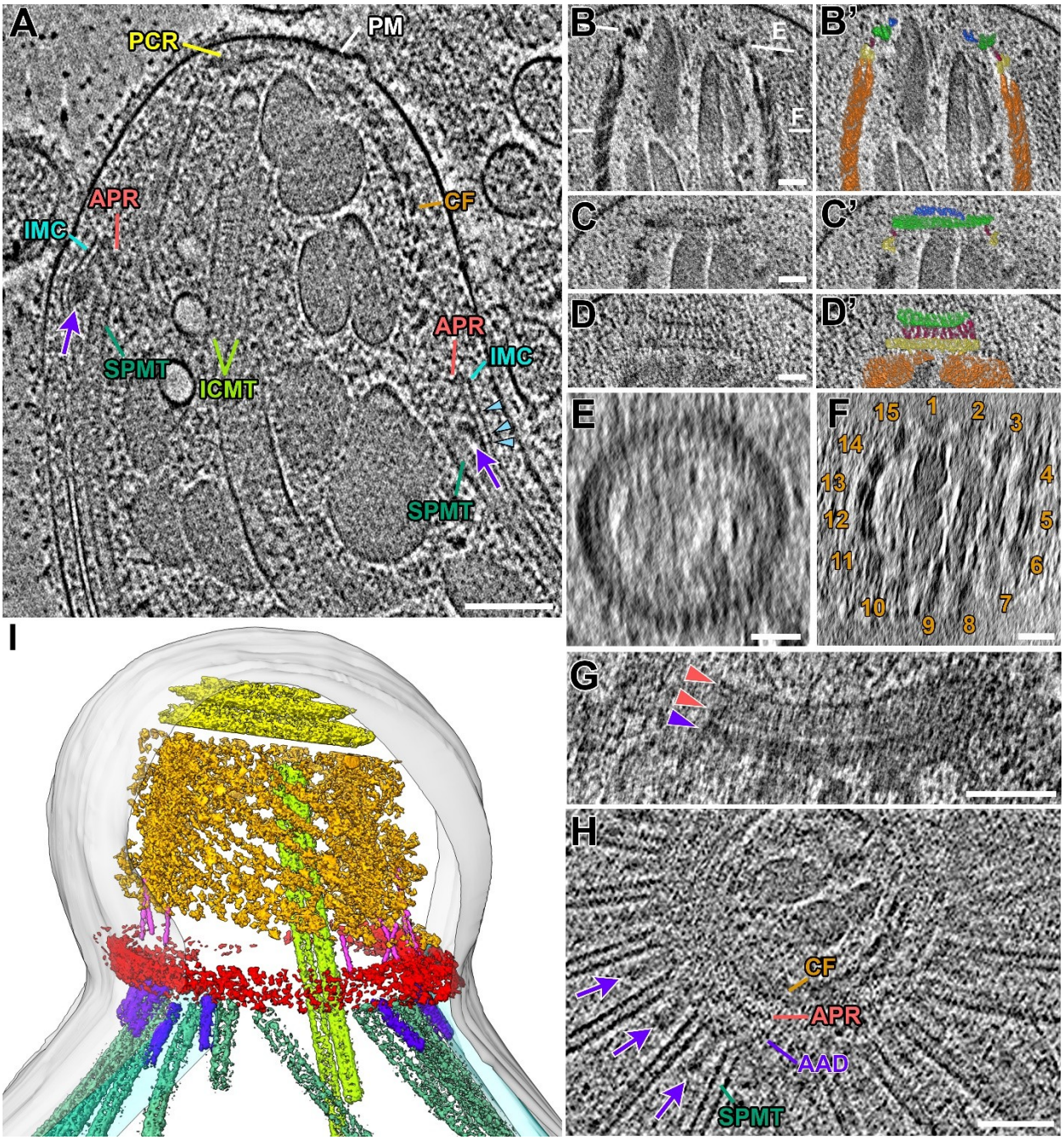
A
PCR
PM
APR
IMC
CF
SPMT
ICMT
APR
IMC
SPMT
B
E
F
B'
C
C'
D
D'
E
F
15
1
2
3
14
4
13
5
12
6
11
7
10
9
8
I
G
H
CF
APR
AAD
SPMT

Figure 1.

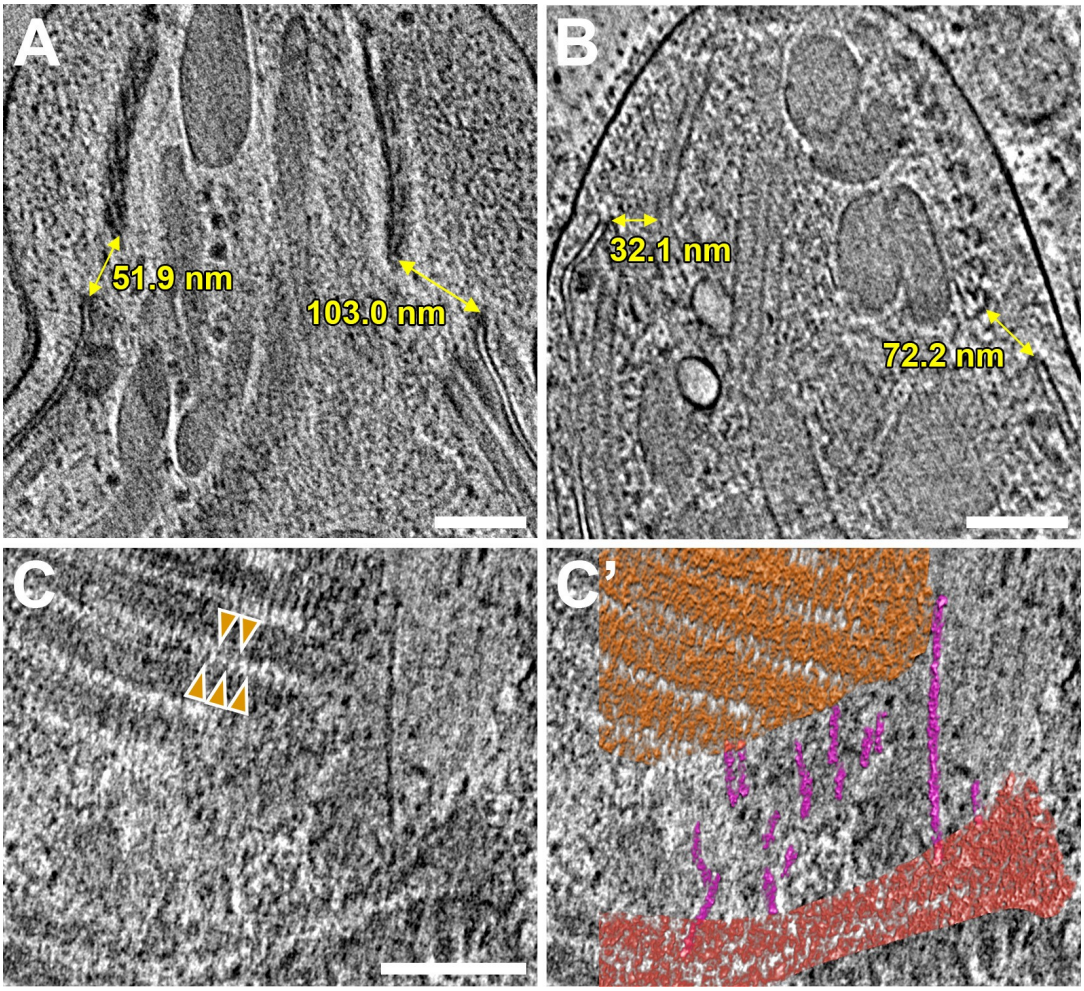

Figure 2.

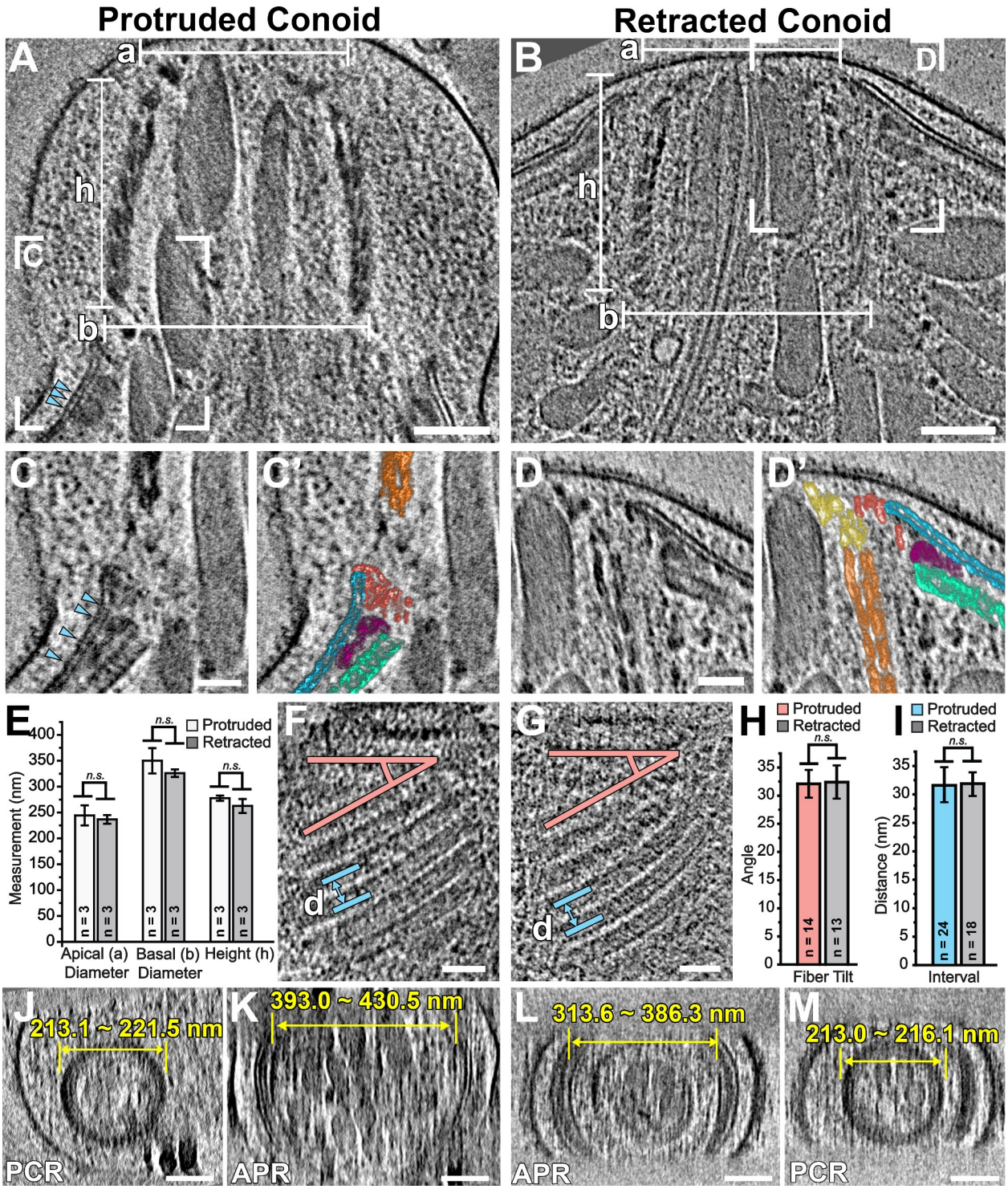
Protruded Conoid
Retracted Conoid
A
B
a
b
h
C
D
C'
D'
E
F
G
H
I
Protruded
Retracted
n.s.
Measurement (nm)
Apical (a) Diameter
Basal (b) Diameter
Height (h)
n = 3
d
Angle
Fiber Tilt
n = 14
n = 13
Distance (nm)
Interval
n = 24
n = 18
J
K
L
M
213.1 ~ 221.5 nm
393.0 ~ 430.5 nm
313.6 ~ 386.3 nm
213.0 ~ 216.1 nm
PCR
APR

Figure 3.

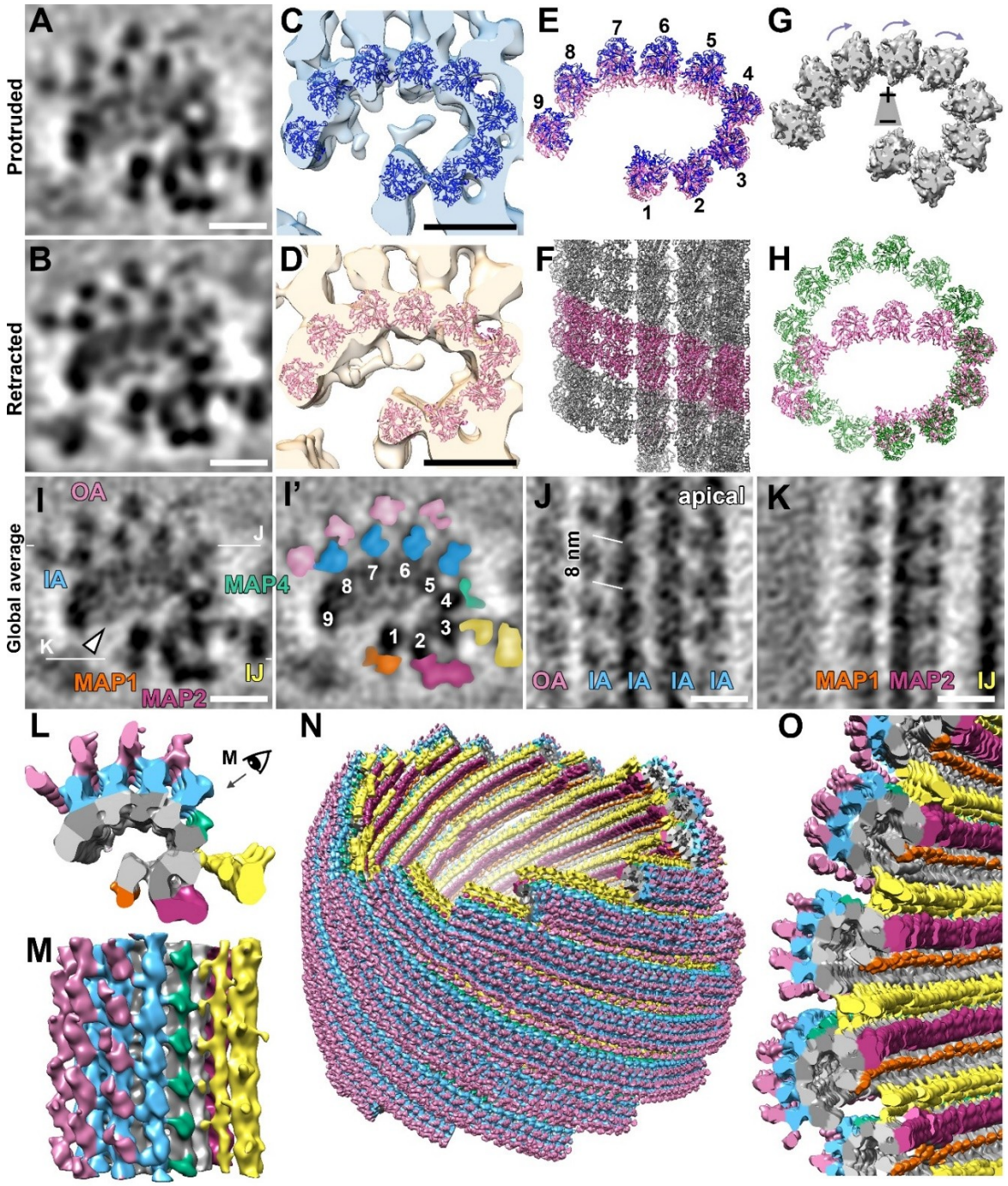
A
C
E
G
Protruded
B
D
F
H
Retracted
I
OA
J
IA
MAP4
K
MAP1
MAP2
IJ
I'
J
apical
8 nm
OA
IA
IA
IA
IA
K
MAP1
MAP2
IJ
Global average
L
M
N
O
M

Figure 4.

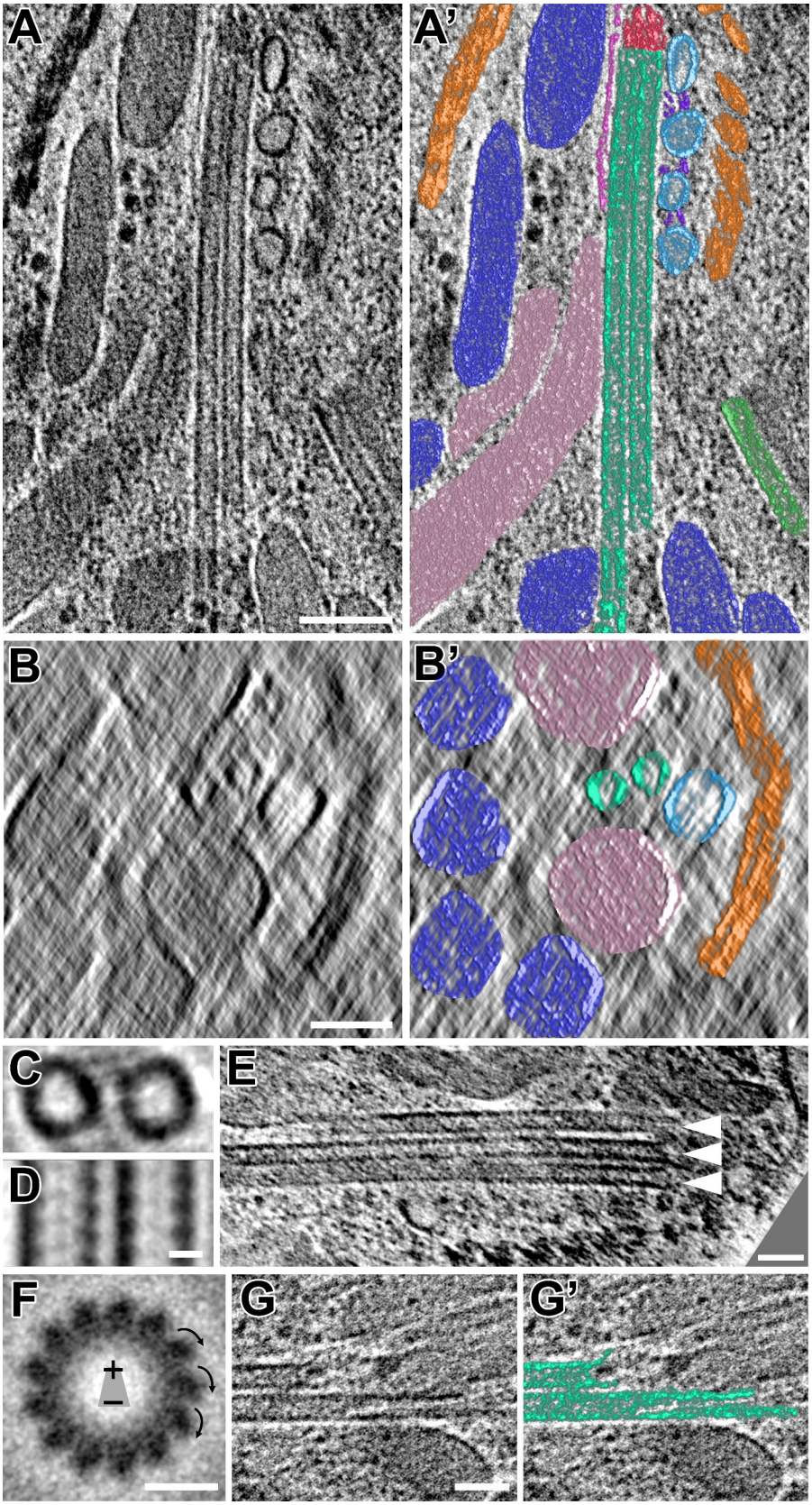

Figure 5.

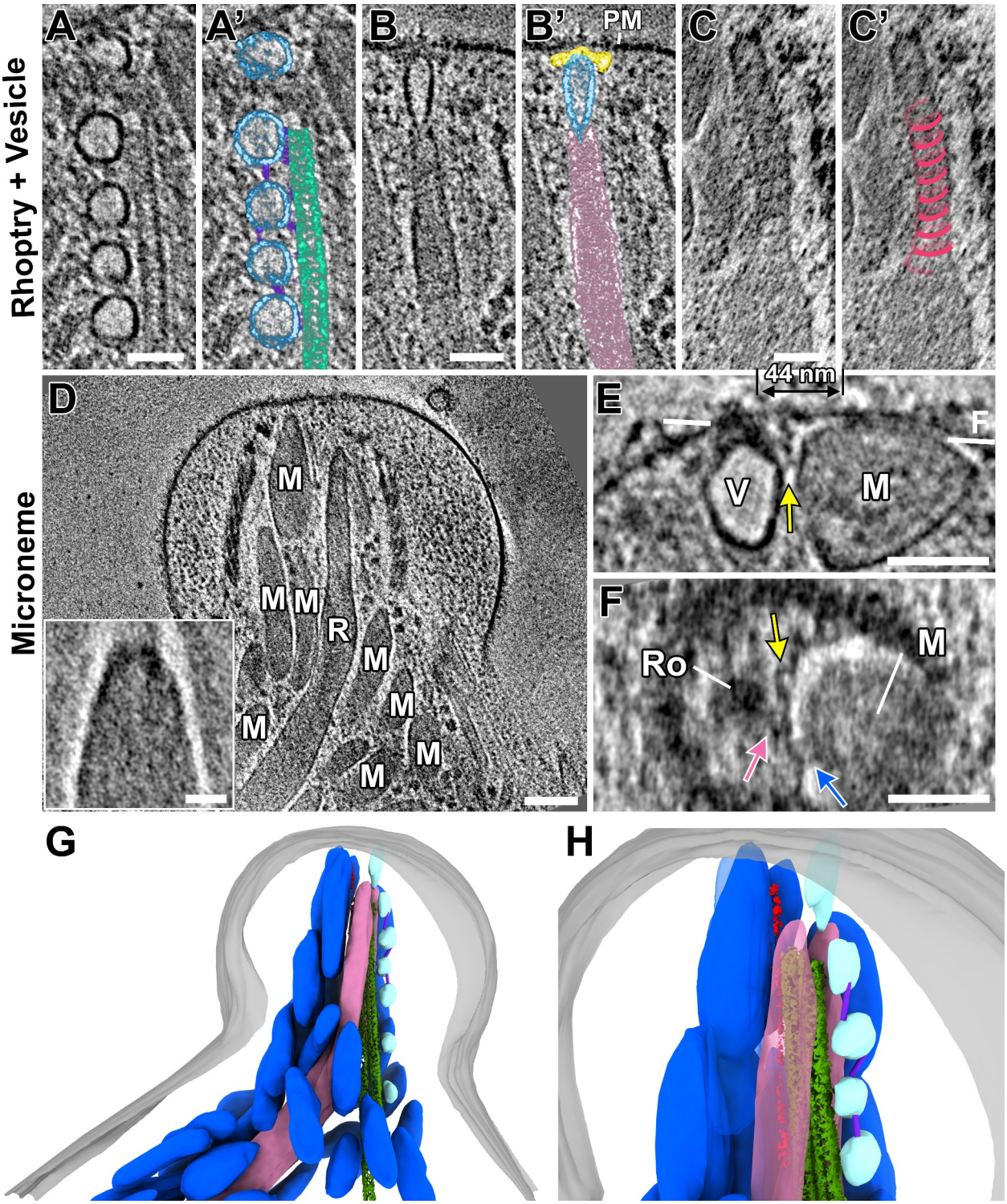
Rhoptry + Vesicle
Microneme
A
A'
B
B'
PM
C
C'
D
M
M M
R
M
M
M
M
M
E
44 nm
F
V
M
F
Ro
M
G
H

Figure 6.

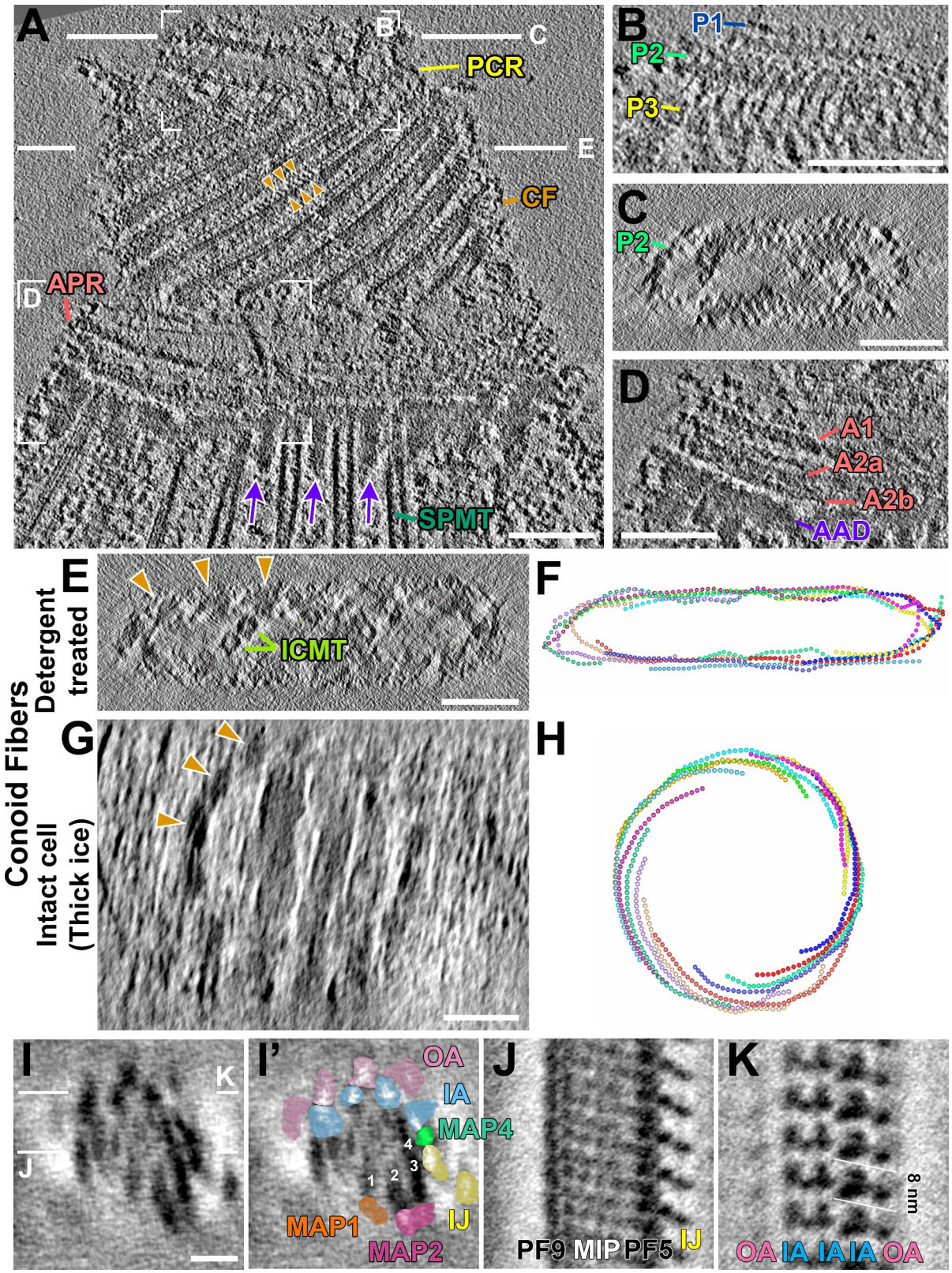
A
B
C
PCR
E
CF
D
APR
SPMT
B
P1
P2
P3
C
P2
D
A1
A2a
A2b
AAD
Conoid Fibers
Detergent treated
E
ICMT
F
Intact cell (Thick ice)
G
H
I
K
J
I'
OA
IA
MAP4
4
3
2
1
MAP1
MAP2
IJ
J
PF9 MIP PF5
IJ
K
8 nm
OA IA IA IA OA

Figure S1.

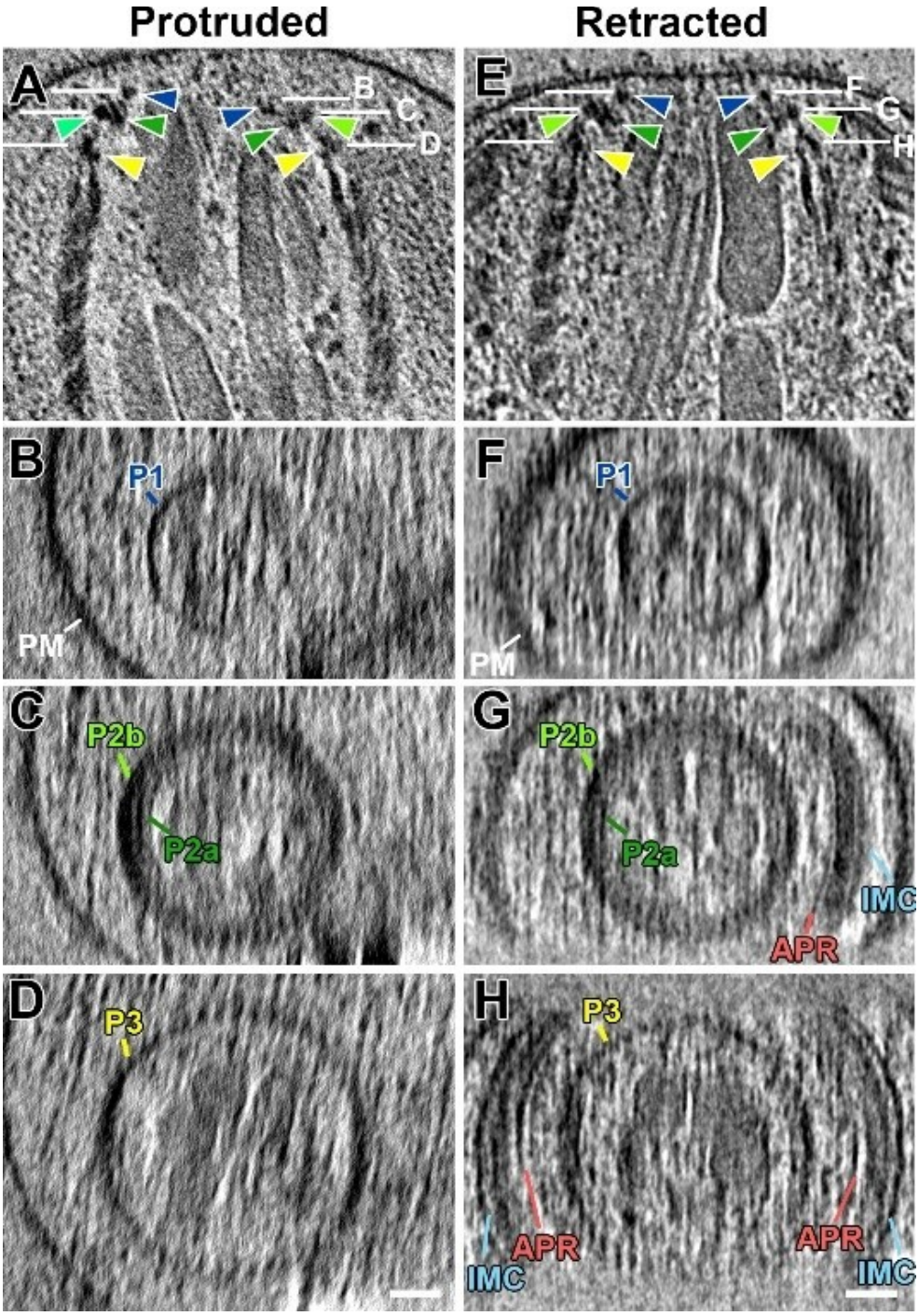

Figure S2.

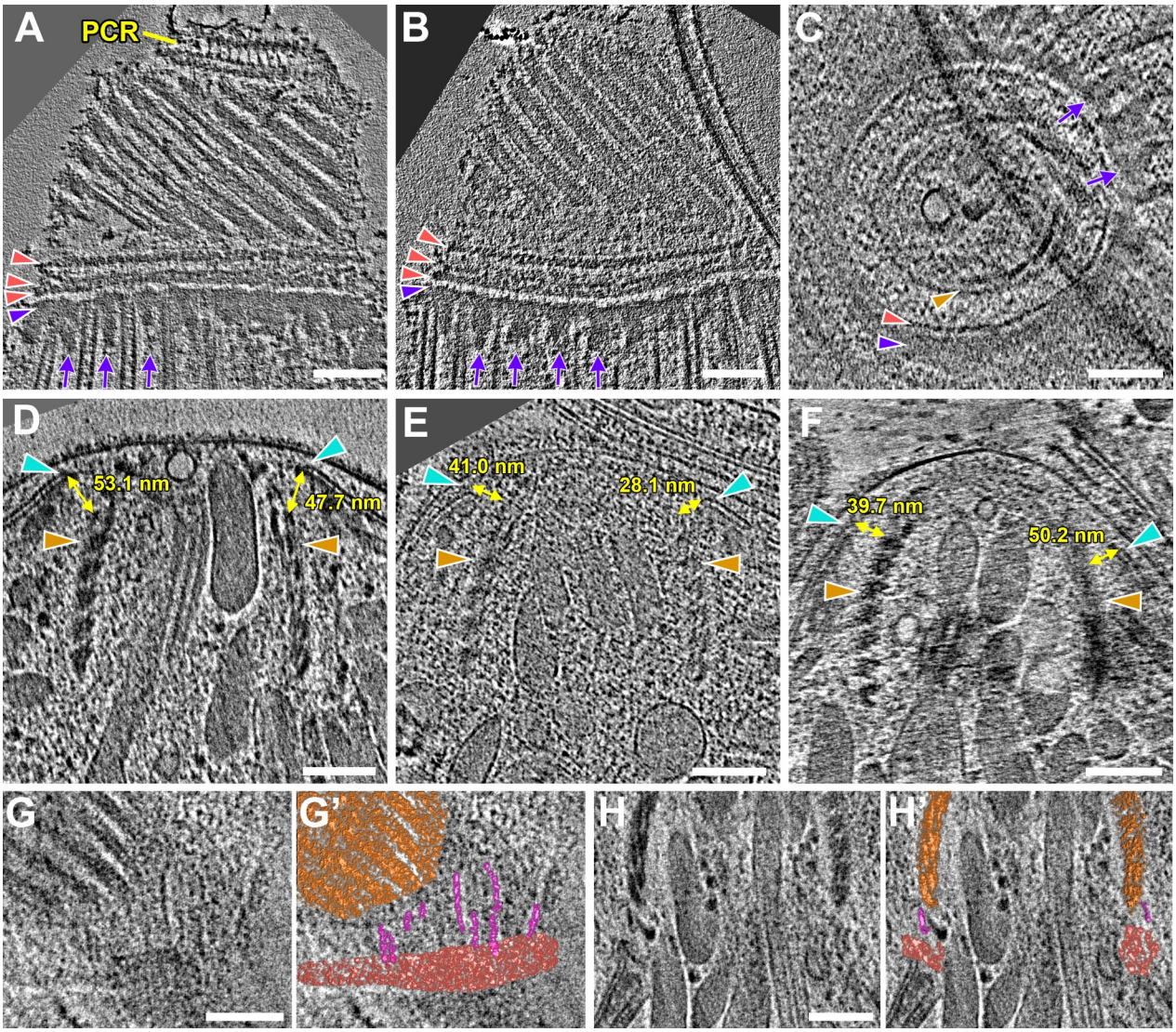

Figure S3.

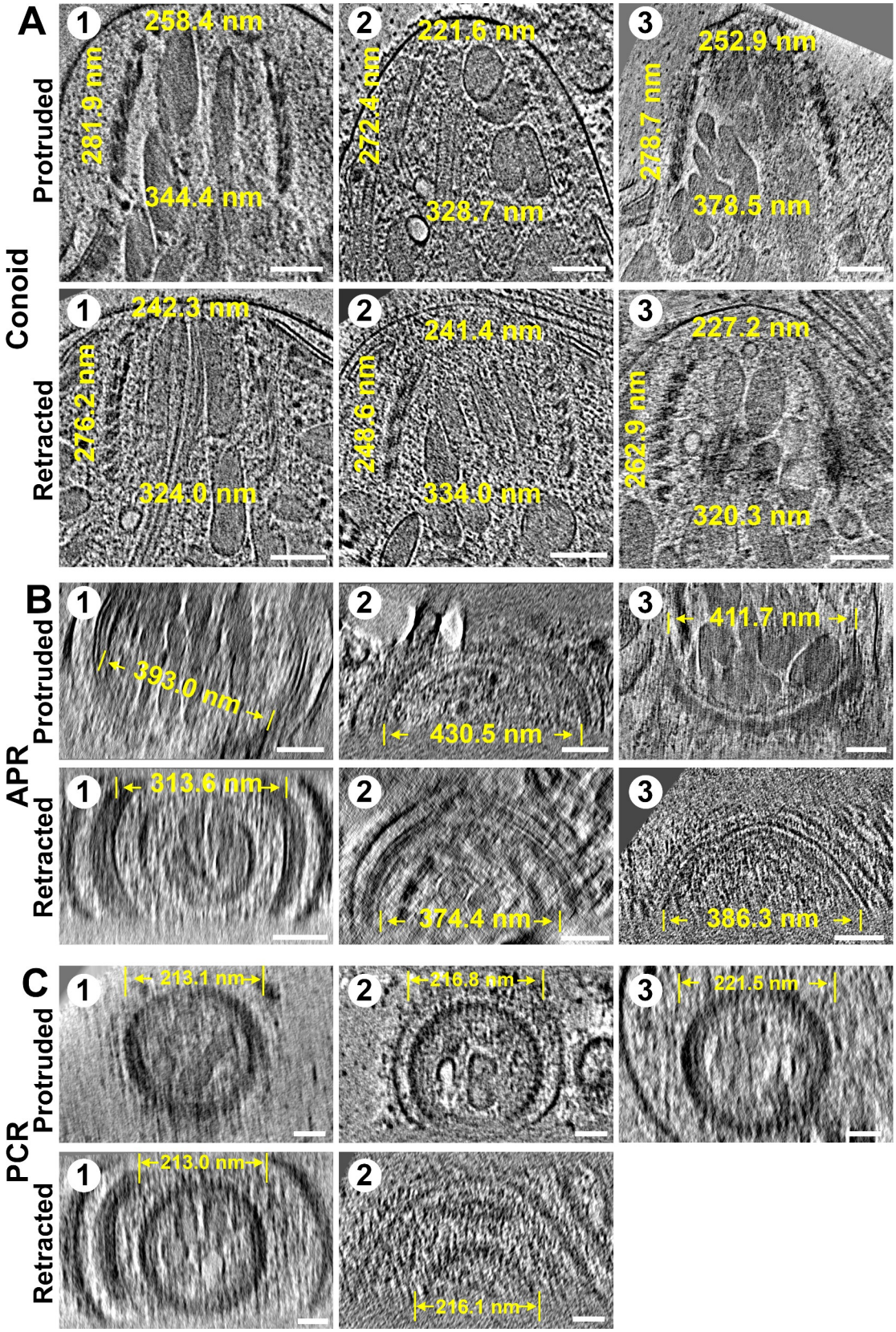
A
Conoid
Protruded
Retracted
1
258.4 nm
281.9 nm
344.4 nm
2
221.6 nm
272.4 nm
328.7 nm
3
252.9 nm
278.7 nm
378.5 nm
1
242.3 nm
276.2 nm
324.0 nm
2
241.4 nm
248.6 nm
334.0 nm
3
227.2 nm
262.9 nm
320.3 nm
B
APR
Protruded
Retracted
1
393.0 nm
2
430.5 nm
3
411.7 nm
1
313.6 nm
2
374.4 nm
3
386.3 nm
C
PCR
Protruded
Retracted
1
213.1 nm
2
216.8 nm
3
221.5 nm
1
213.0 nm
2
216.1 nm

Figure S4.

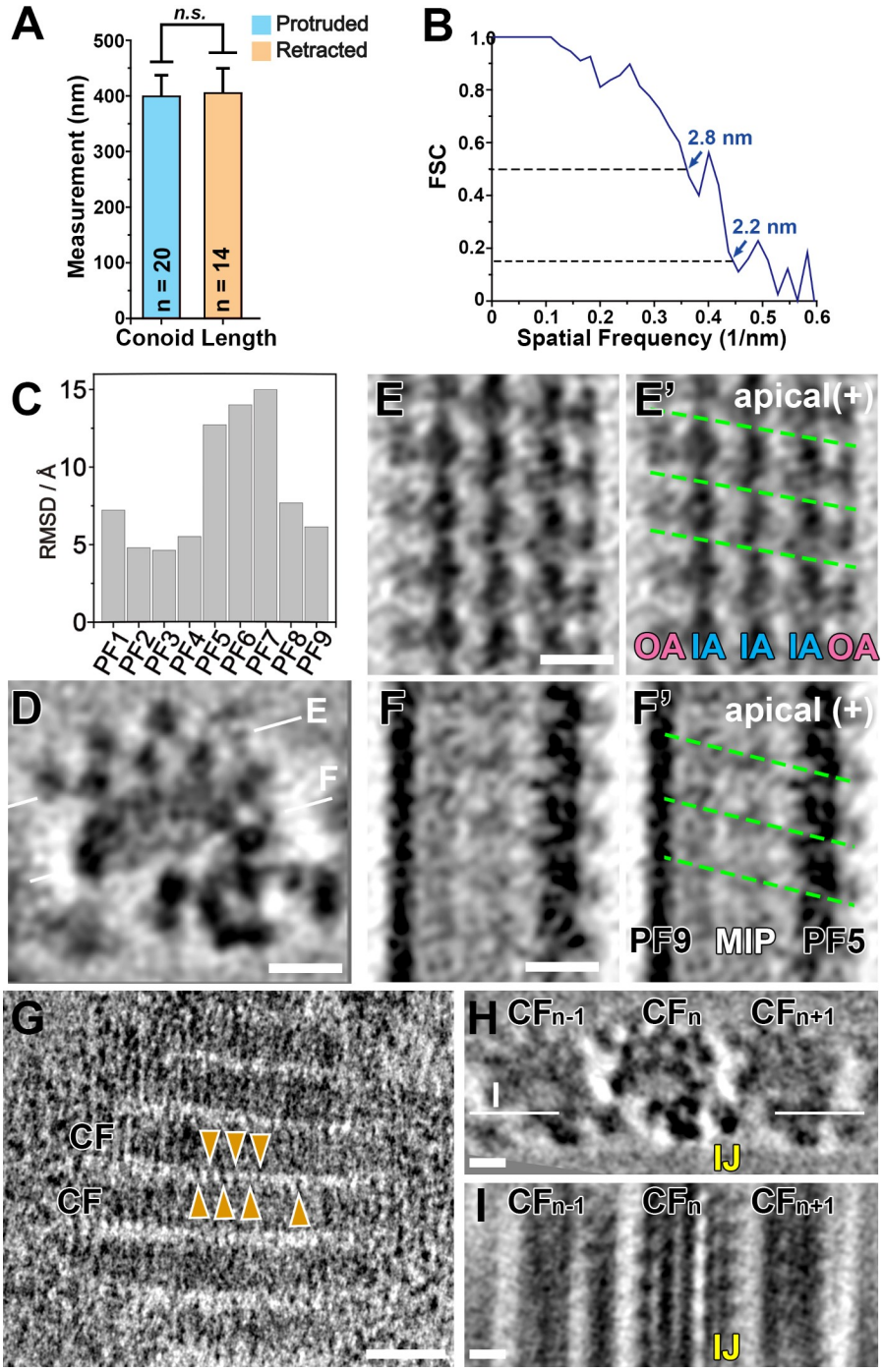
A
n.s.
Protruded
Retracted
Measurement (nm)
500
400
300
200
100
0
n = 20
n = 14
Conoid Length
B
FSC
1.0
0.8
0.6
0.4
0.2
0
2.8 nm
2.2 nm
0
0.1
0.2
0.3
0.4
0.5
0.6
Spatial Frequency (1/nm)
C
RMSD / Å
15
10
5
0
PF1
PF2
PF3
PF4
PF5
PF6
PF7
PF8
PF9
E
E'
apical(+)
OA IA IA IA OA
D
E
F
F
F'
apical (+)
PF9 MIP PF5
G
CF
CF
H
CFn-1
CFn
CFn+1
I
IJ
I
CFn-1
CFn
CFn+1
IJ

Figure S5.

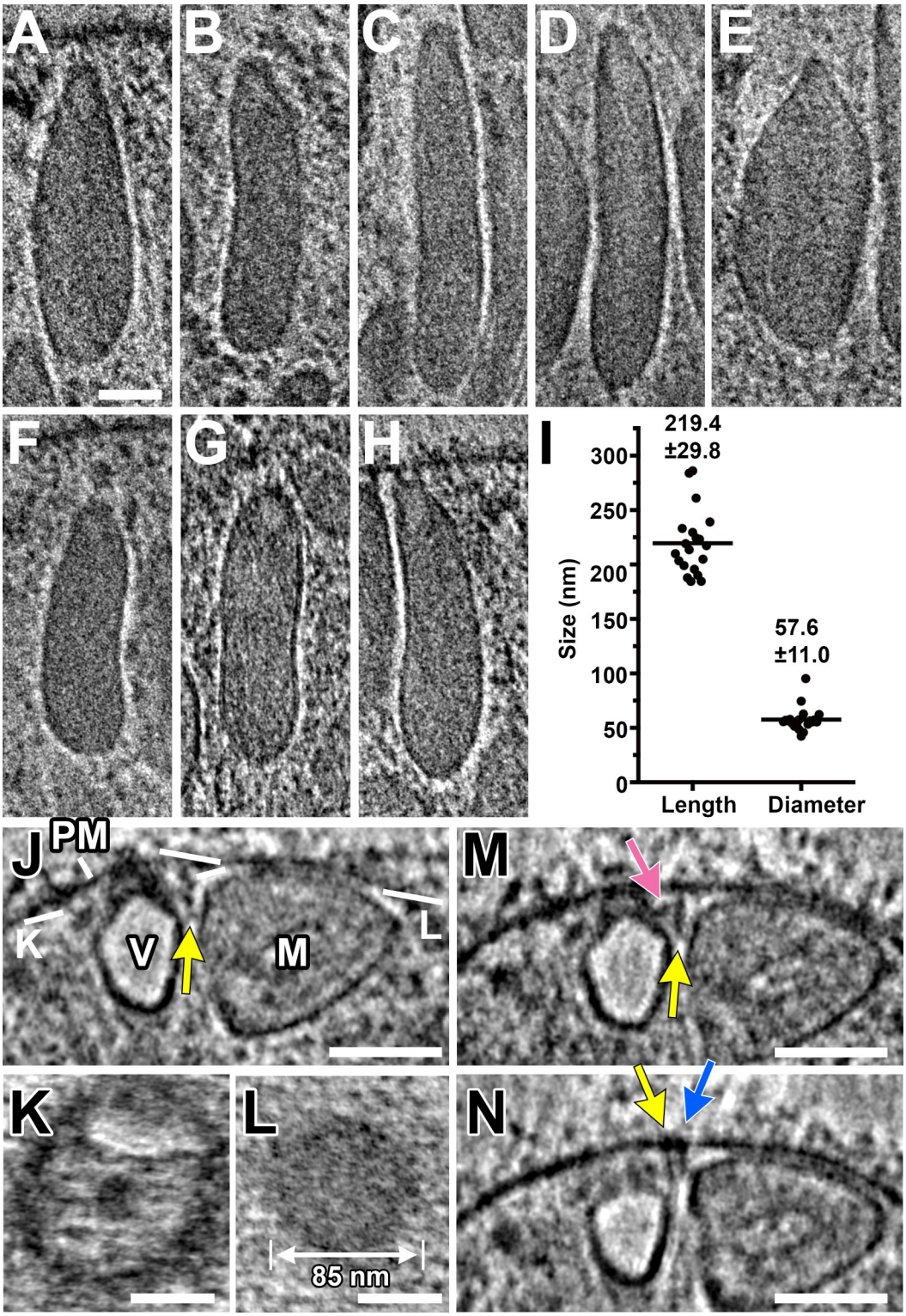
A
B
C
D
E
F
G
H
I
219.4
±29.8
57.6
±11.0
Size (nm)
300
250
200
150
100
50
0
Length
Diameter
J
PM
K
V
M
L
M
K
L
85 nm
N

Figure S6.